Physics of Fluids

RESEARCH ARTICLE | NOVEMBER 14 2023

A fully Eulerian two-layer model for the simulation of oil spills spreading over coastal flows

Special Collection: Recent Advances in Marine Hydrodynamics

I. Echeverribar ; P. Brufau ; P. García-Navarro

Physics of Fluids 35, 116602 (2023)
https://doi.org/10.1063/5.0169493

Physics of Fluids ARTICLE pubs.aip.org/aip/pof

A fully Eulerian two-layer model for the simulation of oil spills spreading over coastal flows

Cite as: Phys. Fluids **35**, 116602 (2023); doi: 10.1063/5.0169493
Submitted: 26 July 2023 · Accepted: 3 October 2023 ·
Published Online: 14 November 2023

I. Echeverribar,[1,2,a)] P. Brufau,[1] and P. García-Navarro[1]

AFFILIATIONS

[1]I3A, University of Zaragoza, Zaragoza, Spain
[2]Hydronia Europe, S. L., Madrid, Spain

Note: This paper is part of the special topic, Recent Advances in Marine Hydrodynamics.
[a)]**Author to whom correspondence should be addressed:** echeverribar@unizar.es

ABSTRACT

Nowadays, the vast majority of coastal oil spill simulation models are based on Lagrangian methods focused on particle tracking algorithms to represent the oil slick fate. In this work, a fully Eulerian numerical model for the simulation of such environmentally significant disaster is implemented by means of a two-dimensional two-layer shallow water model. A very thin oil layer over a thicker water layer is considered in order to neglect the pressure term that the oil layer exerts over the water. Friction terms between layers are responsible for the layers coupling so that the oil layer flows over a moving water volume. To complete this dynamic model, the temperature transport and evolution under heat exchange for the oil upper layer is considered and the weathering process of evaporation is included. The numerical solution adopted is based on a finite volume upwind scheme with a Roe solver for both oil and water layers. Special care has been taken on the numerical treatment of the two-layer wet-dry boundaries (oil–water–land) and friction terms, since the objective of the model is to compute the oil slick front advancing near the coast.

I. INTRODUCTION

Oil spills are environmental disasters that can have far-reaching impacts, disrupting the balance of the marine and coastal ecosystem. When an oil spill occurs, a thin oil film covers the water surface preventing sunlight from passing through water and causing significant harm to the marine ecosystem. One of the primary impacts of oil spills is the generation of toxicity, which can result in the death of marine organisms that affected their ability to breathe, feed, and reproduce. As the oil slick spreads, it can create other environmental problems, such as the destruction of shoreline habitats and the contamination of water supplies. According to data from the International Tanker Owners Pollution Federation (ITOPF), in 2022, there were seven recorded incidents, with three of them categorized as "large" spills due to their spillage exceeding 700 ton. In total, the cumulative amount of oil released into the environment from tanker accidents in 2022 was around 15 000 ton, with over 14 000 ton stemming from those three large incidents.[1]

The occurrence of oil spills poses significant challenges to society, requiring the development of effective strategies for protection and response. The establishment of clear priorities for protection is crucial for maximizing the efficient use of mitigating resources, such as booms, to limit the extent of oil spread. In this regard, understanding the evolving nature of an oil spill becomes crucial. According to a survey conducted by the ITOPF,[2] the ability to predict the behavior of oil spills plays a vital role in determining the most effective response measures.

Traditionally, oil spills containment decisions have relied on aerial images and SAR satellite observations,[3] where the identification of thicker oil areas is useful for the allocation of resources and corrective actions proposals. However, these methods often rely solely on the visual assessment of oil color, which may not provide an accurate representation of the real oil thickness.[3] The ITOPF's report highlights the limitations of this method based only on aerial images and emphasizes the value of incorporating simulation models for a more comprehensive understanding of the extent and thickness of oil pollution.

The modelization of oil spills as an alternative to observations has a long trajectory and has received different contributions along the years. Earlier works were focused on the development of empirical laws for the maximum extension of an oil slick, requiring usually a previous estimation of the distribution of some variables, such as the oil slick thickness.[4]

Afterward, some models were developed focused on the weathering processes and the interactions between the oil and the shoreline[4]

using simplified methodologies for the problem dynamics. While these simplified models may be useful in situations where observational or modeling constraints exist, they often fail to capture the full significance and complexity of the environmental conditions, such as currents or winds. A few models are based on some simplified kinematic equations that, however, need to be numerically solved.[4–6] In some other cases, the models only take care of the computation of the oil slick extension, and thickness, assuming the dynamics as an input. However, in order to advance the understanding of the underlying governing processes, models should prioritize explicit descriptions of the dynamics occurring at the coastline.[4]

For this reason, in recent years, significant contributions have been made in the field of oil spill modeling[7] and their dynamics. The majority of numerical models available for oil spill dynamics modeling can be divided into two different groups: Eulerian and Lagrangian models. Eulerian approaches are based on the modelization of the oil slick through physical conservation laws,[8] while Lagrangian models rely on the use of a large set of particles that are transported by the combined effects of wind, water currents, waves, and diffusion, effectively representing the movement and behavior of oil slicks under a given velocity field representing the water behavior. Focusing on particle tracking algorithms to represent the movement and behavior of oil slicks, they are simpler than Eulerian models and, thus, require less computational effort. However, these Lagrangian-based approaches often overlook the interplay between the oil layer and the underlying water dynamics, limiting their ability to capture the intricate processes involved in oil spill spreading.[8,9]

In either case (whether Lagrangian or Eulerian), these advanced models that consider the dynamics with meteorological, hydrodynamic, and wave models often need additional fate mechanisms in order to enable high-resolution and highly accurate forecasts of oil transport and fate. Among all the mechanisms present in oil spreading, the most commonly accounted for processes include spreading, advection, diffusion, evaporation, emulsification, and dispersion,[6,7] frequently neglecting oil dissolution, photo-oxidation, biodegradation, vertical mixing, and sedimentation.

In addition to weathering processes and water dynamics, wind stresses have been traditionally accounted when dealing with free source flows,[10] specially in coastal areas.[11,12] Consequently, in the context of oil spill simulation, the inclusion of wind effect plays a significant role in shaping the behavior of oil spills,[13,14] particularly when considering wind–wave–current interactions (WWCI) in marine environments. For instance, Ref. 14 has shown strong currents and large waves contribute to the expansion of the oil film coverage, while high wind speeds tend to transport oil mass in shallow water areas. Understanding the complex dynamics of wind and its interactions with waves and currents is crucial for accurately predicting oil spill trajectories and designing effective prevention and mitigation strategies in coastal areas and estuaries. By integrating wind effects into the oil spill model, a more accurate representation of real-world scenarios is achieved, capturing the intricate dynamics of oil slicks under varying wind conditions.

In the same sense, the temperature effect is also crucial when trying to simulate oil spills spreading, due to its influence on other variables such as viscosity, density, and evaporation rate.[15] In addition to the rheology of the oil, other oil processes are strongly affected by temperature. However, although the significance of evaporation in oil spills is recognized,[16] there is a gap in understanding the specific physics and chemistry involved. Further research is necessary to develop comprehensive models and equations that account for the complexities of oil evaporation and to improve the accuracy of predicting its effects in different spill scenarios.[16] Although evaporation has been traditionally modeled as a decay with time,[17] nowadays several studies provide more complex models depending on temperature and atmosphere exposure time.[18] As these approximations are calibrated with real events to reproduce the oil evaporation mechanisms,[18] it can be concluded that accurate temperature modeling is essential for capturing the evaporation.

The present work is concerned with a new model for the simulation of oil spills implemented by means of a fully Eulerian 2D two-layer shallow water type model. The depth-averaged mass and momentum conservation equations, solved in both layers, are coupled through the inter-layer friction source terms in which the lower layer acts as the moving bottom of the upper layer, affecting its dynamics. Additionally, the depth-averaged energy equation in the upper layer leads to a transport equation of the oil temperature whose changes affect the oil viscosity and density. Additionally, wind stress, heat exchange, and evaporation are included in the model.

In generic depth-averaged two-layer models, not only friction source terms but also pressure terms provide the coupling mechanism between layers.[19,20] The present model is oriented to relatively thin layers of oil spills. For this reason, one of the new contributions of this model consists in neglecting the pressure term exerted by the upper oil layer over the lower water layer based on dimensional analysis reasons. The coupling pressure terms usually derive into numerical instabilities, as reported by Ref. 19.

Due to the necessity of a local formulation for the evaporation process in terms of local variables and time, global models have been dismissed. In this work, an evaporation model calibrated for a specific oil has been incorporated as an example to account for the evaporation process[16] in the oil (upper) layer. Although there is a recognized need for further improvements and the complex nature of oil compositions poses challenges in formulating precise evaporation equations tailored to specific oil types,[18] the implemented model computes the evaporation with an expression that depends not only on temperature, but also on the *age* of the spilled petroleum, based on the fact that the evaporation process occurs in the first stages of the spillage.[16,18]

In summary, the design of a numerical model based on a thin two-layer assumption for the simulation of the oil and water dynamics of oil spills is presented in this work, together with the additional processes of wind stress, temperature transport, and evaporation that can affect oil spill. To solve this system, a finite volume first order upwind scheme with an augmented Roe solver is used to solve the equations in both layers: oil slick and water column. Special care is taken on the treatment of the two-layer wet-dry mechanisms following[21–23] and the numerical treatment of source term between layers, as the aim of the model is to compute the oil slicks front advance spreading. The treatment of friction source terms in shallow water models has been extensively studied.[24–27] Different numerical strategies have been proposed to address the stability limitations of including friction terms in the numerical schemes. One approach is the use of an additional stability condition governed by friction.[24–26] On the other hand, implicit approaches, which lead to the introduction of friction terms in a cell-centered manner,[27] provide stability although potentially sacrificing

accuracy in preserving steady states. Alternatively, numerical fixes have been proposed to limit the source term strength instead of the time step size[22,23] to gain computational speed. In the context of sensitivity to friction stresses between layers, two options for computing friction source terms are considered in the present work: the pure upwind approach and a semi-implicit discretization.

The outline of this work is as follows: in Sec. II, the set of mass and momentum equations governing the 2D two-layer oil-water movement as well as the energy equation for the oil upper layer temperature and evaporation evolution are presented. Then, in Sec. III, the numerical model used to solve them is summarized with emphasis on the numerical treatment of the friction stresses. The numerical results can be seen in Sec. IV. First, steady state reference solutions are compared with numerical results, as well as mass conservation with evaporation is validated. Next, unsteady test cases are proposed to analyze the performance of the model in complex wet/dry situations involving oil spills over water approaching the land, including wind and evaporation. Finally, concluding remarks can be read in Sec. V.

II. FULLY EULERIAN 2D TWO-LAYER GOVERNING EQUATIONS

Oil and water flow at each layer, upper and lower, are assumed to be governed by a set of depth-averaged shallow water (SW) equations coupled through friction terms in the momentum equations.[19] For each of the layers, the SW system contains the vertical depth-averaged 2D mass and momentum conservation equations. As depicted in Fig. 1, from now on, subindex 1 will refer to the upper layer corresponding to the oil flow, while subindex 2 will refer to the lower layer corresponding to the water flow. Therefore, assuming constant density, equations for each layer, $L = (1, 2)$, are written as follows:

$$\frac{\partial h_L}{\partial t} + \frac{\partial (h_L u_L)}{\partial x} + \frac{\partial (h_L v_L)}{\partial y} = \theta f_{evap}, \tag{1a}$$

$$\frac{\partial (h_L u_L)}{\partial t} + \frac{\partial}{\partial x}\left(h_L u_L^2 + \frac{1}{2} g h_L^2\right) + \frac{\partial (h_L u_L v_L)}{\partial y} = -\frac{h_L}{\rho_L}\frac{\partial p_{sL}}{\partial x} - g h_L \frac{\partial z_{bL}}{\partial x} + \frac{\tau_{sL}}{\rho_L} + \frac{\tau_{bL}}{\rho_L}, \tag{1b}$$

$$\frac{\partial (h_L v_L)}{\partial t} + \frac{\partial (h_L u_L v_L)}{\partial x} + \frac{\partial}{\partial y}\left(h_L v_L^2 + \frac{1}{2} g h_L^2\right) = -\frac{h_L}{\rho_L}\frac{\partial p_{sL}}{\partial y} - g h_L \frac{\partial z_{bL}}{\partial y} + \frac{\tau_{sL}}{\rho_L} + \frac{\tau_{bL}}{\rho_L}, \tag{1c}$$

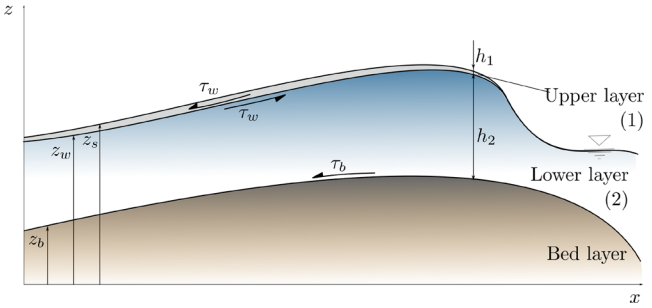

FIG. 1. Profile of the 2D two-layer system considered in this work.

where h_L and ρ_L are the layer depth and density, respectively; $\mathbf{u}_L = (u_L, v_L)$ are the x and y components of the velocity vector; $h_L u_L$ and $h_L v_L$ stand for the corresponding unit discharges in each spatial horizontal direction; p_{sL} represents the pressure; z_{bL} is the reference bottom depth for each layer; and τ_{sL} and τ_{bL} are viscous and bed friction stresses. Finally, f_{evap} stands for the evaporation rate in the oil and is multiplied by θ, which is $\theta = 0$ for the lower layer (L = 2) and $\theta = 1$ for the upper layer (L = 1).

The boundary conditions on the different surfaces are given in the following:

For the upper layer (L = 1):

- At $z = z_{s1} = z_s$, p_{s1} is assumed to be the atmospheric pressure by neglecting surface tension effects, $p_{s1} = p_{atm} = 0$.
- At $z = z_{s1} = z_s$, the viscous stress can be modeled as the friction exerted by wind, to be defined as τ_a.
- At $z = z_{b1} = z_w$, the pressure is represented by the same value at the bottom level of the upper layer that coincides with the upper surface of lower layer (L = 2), which is $z_{b1} = z_{s2} = z_{b2} + h_2$.
- At $z = z_{b1} = z_w$, the bed friction stress is imposed as τ_w.

For the lower layer (L = 2):

- At $z = z_{s2} = z_w$, p_{s2} is the pressure exerted by the upper column of oil at the interface, $p_{s2} = p_1(z_{b1}) = p_{atm} + \rho_1 g h_1$.
- At $z = z_{s2} = z_w$, the surface shear stress is the friction with the upper layer, also modeled as $-\tau_w$.
- At $z = z_{b2} = z_b$, the bottom level coincides with the bed layer level, which is $z_{b2} = z_b$.
- At $z = z_{b2} = z_b$, the bed friction stress is the friction with the bed layer, modeled as τ_b.

Therefore, the final 2D two-layer system of equations is

$$\frac{\partial h_1}{\partial t} + \frac{\partial (h_1 u_1)}{\partial x} + \frac{\partial (h_1 v_1)}{\partial y} = \theta f_{evap}, \tag{2a}$$

$$\frac{\partial (h_1 u_1)}{\partial t} + \frac{\partial}{\partial x}\left(h_1 u_1^2 + \frac{1}{2} g h_1^2\right) + \frac{\partial (h_1 u_1 v_1)}{\partial y} = -g h_1 \left(\frac{\partial h_2}{\partial x} + \frac{\partial z_b}{\partial x}\right) + \frac{\tau_a}{\rho_1} + \frac{\tau_w}{\rho_1}, \tag{2b}$$

$$\frac{\partial (h_1 v_1)}{\partial t} + \frac{\partial (h_1 u_1 v_1)}{\partial x} + \frac{\partial}{\partial y}\left(h_1 v_1^2 + \frac{1}{2} g h_1^2\right) = -g h_1 \left(\frac{\partial h_2}{\partial y} + \frac{\partial z_b}{\partial y}\right) + \frac{\tau_a}{\rho_1} + \frac{\tau_w}{\rho_1}, \tag{2c}$$

$$\frac{\partial h_2}{\partial t} + \frac{\partial (h_2 u_2)}{\partial x} + \frac{\partial (h_2 v_2)}{\partial y} = 0, \tag{2d}$$

$$\frac{\partial (h_2 u_2)}{\partial t} + \frac{\partial}{\partial x}\left(h_2 u_2^2 + \frac{1}{2} g h_2^2\right) + \frac{\partial (h_2 u_2 v_2)}{\partial y} = -\frac{\rho_1}{\rho_2} g h_2 \frac{\partial h_1}{\partial x} - g \frac{\partial z_b}{\partial x} - \frac{\tau_w}{\rho_2} + \frac{\tau_b}{\rho_2}, \tag{2e}$$

$$\frac{\partial (h_2 v_2)}{\partial t} + \frac{\partial (h_2 u_2 v_2)}{\partial x} + \frac{\partial}{\partial y}\left(h_2 v_2^2 + \frac{1}{2} g h_2^2\right) = -\frac{\rho_1}{\rho_2} g h_2 \frac{\partial h_1}{\partial y} - g \frac{\partial z_b}{\partial y} - \frac{\tau_w}{\rho_2} + \frac{\tau_b}{\rho_2}. \tag{2f}$$

A. The 2D two-layer oil-water model under an oil thin layer assumption

The system of equations (2) represents a generic 2D two-layer model. However, for its application to oil spill simulation, where the upper layer represents a very thin layer, the pressure exerted by the upper layer over the lower one can be neglected.

The estimation of the relative size of the gravity terms in the lower layer momentum equation depends on the relative size of h_1 in comparison with h_2 and the characteristic length of the problem, represented with ℓ, as

$$\frac{-h_2 g \frac{h_1}{\ell}}{g \frac{h_2^2}{\ell}} = \frac{h_1}{h_2} \ll 1. \tag{3}$$

Since in this work, the oil layer is considered much thinner than the water layer, this term is neglected, and system of equations (2) is simplified to

$$\frac{\partial h_1}{\partial t} + \frac{\partial (h_1 u_1)}{\partial x} + \frac{\partial (h_1 v_1)}{\partial y} = \theta f_{evap}, \tag{4a}$$

$$\frac{\partial (h_1 u_1)}{\partial t} + \frac{\partial}{\partial x}\left(h_1 u_1^2 + \frac{1}{2} g h_1^2\right) + \frac{\partial (h_1 u_1 v_1)}{\partial y} = -g h_1 \left(\frac{\partial h_2}{\partial x} + \frac{\partial z_b}{\partial x}\right) + \frac{\tau_a}{\rho_1} + \frac{\tau_w}{\rho_1}, \tag{4b}$$

$$\frac{\partial (h_1 v_1)}{\partial t} + \frac{\partial (h_1 u_1 v_1)}{\partial x} + \frac{\partial}{\partial y}\left(h_1 v_1^2 + \frac{1}{2} g h_1^2\right) = -g h_1 \left(\frac{\partial h_2}{\partial y} + \frac{\partial z_b}{\partial y}\right) + \frac{\tau_a}{\rho_1} + \frac{\tau_w}{\rho_1}, \tag{4c}$$

$$\frac{\partial h_2}{\partial t} + \frac{\partial (h_2 u_2)}{\partial x} + \frac{\partial (h_2 v_2)}{\partial y} = 0, \tag{4d}$$

$$\frac{\partial (h_2 u_2)}{\partial t} + \frac{\partial}{\partial x}\left(h_2 u_2^2 + \frac{1}{2} g h_2^2\right) + \frac{\partial (h_2 u_2 v_2)}{\partial y} = -g \frac{\partial z_b}{\partial x} - \frac{\tau_w}{\rho_2} + \frac{\tau_b}{\rho_2}, \tag{4e}$$

$$\frac{\partial (h_2 v_2)}{\partial t} + \frac{\partial (h_2 u_2 v_2)}{\partial x} + \frac{\partial}{\partial y}\left(h_2 v_2^2 + \frac{1}{2} g h_2^2\right) = -g \frac{\partial z_b}{\partial y} - \frac{\tau_w}{\rho_2} + \frac{\tau_b}{\rho_2}. \tag{4f}$$

At this point, friction stresses need to be defined to close system (4): the basal stress $\boldsymbol{\tau_b}$ (Pa), affecting mainly the lower layer—unless $h_2 = 0$—, the wind stress $\boldsymbol{\tau_a}$ (Pa), which affects the upper layer in the most general case—unless $h_1 = 0$—, and the interface stress between the two layers, $\boldsymbol{\tau_w}$ (Pa). All are expressed in the equations by means of their components as

$$\boldsymbol{\tau_b} = (\tau_{bx}, \tau_{by}) = \tau_b \, \mathbf{n_{uL}}, \tag{5a}$$

$$\boldsymbol{\tau_w} = (\tau_{wx}, \tau_{wy}) = \tau_w \, \mathbf{n_{ur,w}}, \tag{5b}$$

$$\boldsymbol{\tau_a} = (\tau_{ax}, \tau_{ay}) = \tau_a \, \mathbf{n_{ur,a}}, \tag{5c}$$

with $\mathbf{n_u} = (n_{ux}, n_{uy})$ the direction given by the velocity unit vector, which is different depending on the layer. For stresses affecting only one layer, L, such as bed friction, it is based on the layer velocity as

$$\mathbf{n}_{uL} = (n_{uLx}, n_{uLy}) = \left(\frac{u_L}{|\mathbf{u}_L|}, \frac{v_L}{|\mathbf{u}_L|}\right). \tag{6}$$

When computing the interface stress, the unit velocity vector is computed with the relative velocity between layers

$$\mathbf{n}_{ur,w} = (n_{ur,w,x}, n_{ur,w,y}) = \left(\frac{u_{r,w}}{|\mathbf{u}_{r,w}|}, \frac{v_{r,w}}{|\mathbf{u}_{r,w}|}\right), \tag{7}$$

being $\mathbf{u}_{r,w} = \mathbf{u}_1 - \mathbf{u}_2$, the relative velocity between layers. At this point, it is important to mention that this model comes from an empirical formula. However, when dealing with two fluids of different densities and velocities at an interface, shear stress across the interface due to the velocity difference and density contrast could be more complex. In any case, not only the differences in densities of oil and water and the differences on velocities in the vast majority of application cases are not such big, but also is important to note that the aim of this work is the numerical validation and robustness analysis of the model. Thus, the most accurate validation with more complex models is out of scope of this work.

On the other hand, in the interface between fluid and air,

$$\mathbf{n}_{ur,a} = (n_{ur,a,x}, n_{ur,a,y}) = \left(\frac{u_{r,a}}{|\mathbf{u}_{r,a}|}, \frac{v_{r,a}}{|\mathbf{u}_{r,a}|}\right), \tag{8}$$

being $\mathbf{u}_{r,a} = \mathbf{u}_a - \mathbf{u}_L$, the relative velocity between the air and the layer affected by wind, L.

For the formulation of the basal shear stress, a turbulent friction model has been used in the present work,

$$\tau_b = \rho_L g h_L C_{fn} |\mathbf{u}_L|^2, \tag{9}$$

where $|\mathbf{u}_L| = \sqrt{u_L^2 + v_L^2}$ is the depth-averaged velocity modulus, and C_{fn} is a friction coefficient. When using Manning's formula, this coefficient takes the form of a flow depth (h_L) function, and a Manning roughness coefficient, n_b (s m$^{1/3}$),[28–31] as

$$C_{fn} = \frac{n_b^2}{h_L^{4/3}}. \tag{10}$$

On the other hand, the friction between layers, τ_w, follows a Chézy-type formula applied to the shear interface; thus, depending on the square of the relative velocity,

$$\tau_w = \rho_1 g C_{f_1}(\mathbf{u}_{r,w}) |\mathbf{u}_{r,w}| = \rho_2 g C_{f_{w_2}}(\mathbf{u}_{r,w}) |\mathbf{u}_{r,w}|, \tag{11}$$

with $C_{f_2} = r C_{f_1}$, being $r = \rho_1/\rho_2$ the density relation between both layers.

Finally, the friction with air, τ_a, can be modeled through[11,12]

$$\tau_a = \rho_a g C_a(\mathbf{u}_{r,a}) |\mathbf{u}_{r,a}|, \tag{12}$$

where ρ_a stands for the air density, C_a represents the air friction coefficient, and $\mathbf{u}_a$ represents the wind velocity.

B. Oil temperature transport equation and density

In order to include additional processes, such as oil evaporation or fluid rheological behavior changes, most of them governed by temperature, the fluid temperature, T, is added to the list of variables at the upper layer $L = 1$. Afterward, other variables, such as density, ρ, can also be updated as a function of temperature. The temperature

transport in the upper layer can be formulated by an equation derived from the internal energy conservation law[32,33] as

$$\frac{\partial(h_1 T_1)}{\partial t}+\frac{\partial(h_1 u_1 T_1)}{\partial x}+\frac{\partial(h_1 v_1 T_1)}{\partial y}=\frac{\dot{Q}}{\rho_1 C_p}=\mathcal{S}_{\mathcal{T}}, \tag{13}$$

where $\dot{Q}$ is the net heat flux per unit area [W/(m^2)], and C_p [J/(kg °K)] is the oil specific heat coefficient. The heat transfer mechanisms considered in the source term $\mathcal{S}_{\mathcal{T}}$ are

$$\mathcal{S}_{\mathcal{T}}=\frac{\dot{Q}}{\rho C_p}=\frac{\dot{Q}_{cv,a}+\dot{Q}_{cv,w}+\dot{Q}_{rad}}{\rho C_p}, \tag{14}$$

where $\dot{Q}_{rad}$ stands for the received solar radiation (provided directly as an input), and $\dot{Q}_{cv,a}$ and $\dot{Q}_{cv,w}$ represent the convection heat losses with air and water, respectively, defined as

$$\dot{Q}_{cv,a}=h_{c,a}(T-T_{air}), \tag{15a}$$

$$\dot{Q}_{cv,w}=h_{c,w}(T-T_{water}), \tag{15b}$$

where T_{air} and T_{water} are the air and water temperature, respectively, which in this work are considered constant being the oil temperature the only transported and distributed temperature. The convection coefficient, h_c, takes into account the increase in heat transfer due to the motion of the surroundings. Thus, in this case, they are modeled as[34]

$$h_{c,a}=8.55+2.56|\mathbf{u}_{r,a}|, \tag{16a}$$

$$h_{c,w}=8.55+2.56|\mathbf{u}_{r,w}|, \tag{16b}$$

in terms of the wind velocity modulus and the modulus of the relative velocity between the two liquid layers (oil and water). Finally, the net radiation is neglected for the present application.

Finally, the depth-averaged density ρ can be linearly related to the flow averaged temperature along the flow column T as

$$\rho(T)=\rho_0+K(T-T_0), \tag{17}$$

where ρ_0 is the fluid reference density at the reference temperature T_0, and K is a tuning constant specific for each oil.

C. Oil age and evaporation

There are models that represent oil evaporation based on global variables such as the total area of the slick and the time since the spill began.[35] However, the approach adopted here follows another approximation focused on the local process, which calculates evaporation as a function of the oil column properties at each point in space and time, which fits better in discretized models such the designed in this work. Evaporation can depend not only on the fluid properties, such as density, temperature, or viscosity, but also on the surrounding conditions, such as wind velocity, waves, and currents. However, simplified models have been developed focusing on important aspects of the phenomenon being modeled. For this kind of spills, it is well established that evaporation depends on the oil temperature and on the degradation to which it has been subjected during the time it has been exposed to the environment.[18] The evaporation rate present in Eq. (4a), f_{evap}, is the variation of evaporation fraction, F_v, as

$$f_{evap}=\frac{\partial F_v}{\partial t}h. \tag{18}$$

In addition, according to Ref. 18, the evaporated fraction at a point (x, y) at time t, $F_v(x, y, t)$, can be formulated as

$$F_v(x,y,t)=\min\left[(-0.14+0.013T(t,x,y)\sqrt{a(x,y,t)},\mathcal{E}_{\max}\right], \tag{19}$$

where $T(x, y, t)$ is the oil temperature, $\mathcal{E}_{max}$ is the maximum evaporation fraction, which depends on the oil type (in this work, 0.05 is assumed as in Ref. 18), and $a(x, y, t)$ is the age of the oil, which is computed as a transported variable that increases with time. The evolution of this temporal variable is

$$\frac{\partial(h_1 a_1)}{\partial t}+\frac{\partial(h_1 a_1 u_1)}{\partial x}+\frac{\partial(h_1 a_1 v_1)}{\partial y}=h_1\mathcal{X}_c, \tag{20}$$

which represents the transport equation of the depth-averaged oil age a_1 over the oil column depth, h_1. Additionally, $\mathcal{X}_c$ is a source term whose value is 1 where oil depth exists and 0 elsewhere. This means that the value of the oil age a, besides being transported, increases at the same rate as local time. This equation is only considered in the upper layer (layer 1). Diffusion effects are neglected, as the model is applied to situations with strong convection, which is higher than conduction.[33]

III. UPWIND FIRST ORDER NUMERICAL SCHEME AND COMPUTATIONAL DETAILS

The system of equations (4) can be computed independently using a synchronous procedure as the coupling is provided only by the friction source terms τ_w. For that reason, the generic resolution for a SW layer with varying topography and bottom friction is detailed. After that, the particular treatment used in this work for the shear source term between layers τ_w is presented. For the design of the numerical scheme, the system of conservation laws (4) can be written for each layer, L, in a compact way as

$$\frac{\partial \mathbf{U}_L}{\partial t}+\nabla\cdot\mathbf{E}_{\mathbf{L}}(\mathbf{U})=\mathbf{S}_{\mathbf{L},\mathbf{b}}(\mathbf{U})+\mathbf{S}_{L,\tau}(\mathbf{U}), \tag{21}$$

where $\mathbf{U}_L$ stands for the conserved variables vector for layer $L=(1,2)$,

$$\mathbf{U}_L=\begin{pmatrix}h_L & h_L u_L & h_L v_L\end{pmatrix}^T. \tag{22}$$

For the sake of clarity, L is removed from the variables during the following explanation. Accordingly, the conservative fluxes are embedded in $\mathbf{E}(\mathbf{U})=(\mathbf{F}(\mathbf{U}),\mathbf{G}(\mathbf{U}))$,

$$\mathbf{F}(\mathbf{U})=\begin{pmatrix}hu\\ hu^2+\frac{1}{2}gh^2\\ huv\end{pmatrix},\quad \mathbf{G}(\mathbf{U})=\begin{pmatrix}hv\\ huv\\ hv^2+\frac{1}{2}gh^2\end{pmatrix}. \tag{23}$$

$\mathbf{S_b}(\mathbf{U})$ represents the bottom slope source term for each layer, this is, z_b variations for the lower layer and z_b+h_2 for the upper layer. This leads to the definition of a generic layer bottom,

$$\mathcal{Z}_b=z_b+\theta h_2,$$

being $\theta=0$ for the lower layer (L = 2) and $\theta=1$ for the upper layer (L = 1). The other source vector, $\mathbf{S}_{\boldsymbol{\tau}}(\mathbf{U})$, stands for friction stresses that, unless the single layer case is presented, is composed of two different friction stresses acting in the bottom and surface boundaries of

each layer. In particular, for the upper layer $L=1$, it represents wind and interface frictions, while in the lower layer $L=2$, it represents interface and bed friction. Therefore, in a generic way, it can be written as follows: $\mathbf{S}_\tau(\mathbf{U}) = \mathbf{S}_{\tau a}(\mathbf{U}) + \mathbf{S}_{\tau w}(\mathbf{U}) + \mathbf{S}_{\tau b}(\mathbf{U})$, which can be expressed as

$$\mathbf{S_b}(\mathbf{U}) = \begin{pmatrix} 0 \\ -gh(\partial \mathcal{Z}_b/\partial x) \\ -gh(\partial \mathcal{Z}_b/\partial y) \end{pmatrix}, \quad \mathbf{S}_\tau(\mathbf{U}) = \begin{pmatrix} 0 \\ (\tau_a \pm \tau_w - \tau_b)\, n_{ux}/\rho \\ (\tau_a \pm \tau_w - \tau_b)\, n_{uy}/\rho \end{pmatrix}. \tag{24}$$

As mentioned before, the non-linear system (21) is discretized by means of a Godunov type finite volume scheme.[36,37] In the domain, a piecewise uniform distribution of variables is assumed at time level n. The order of the scheme is chosen to be first order as the model, which aims to be applied to real cases, will deal with real coastal topographies, lack of data in parameterized models such those for heat transfer or evaporation, and, thus, it contains too many uncertainties turning higher order methods into useless, besides computationally expensive.

In the 2D framework, the solution is obtained by means of a locally linearized 1D Riemann problem (RP) at each cell edge, k, projected onto the $\mathbf{n}$ direction over an x' axis, following the Roe approach,[22,38] fulfilling the consistency condition.[39] Therefore, the fluxes are evaluated at cell edges as $\delta\mathbf{E} = \mathbf{E}_j - \mathbf{E}_i$, where $\mathbf{E}_j$ is the value of fluxes $\mathbf{E}$ at the neighboring cell j that shares a cell edge, k, of length l_k, with the cell i.

The system (21) has exactly the same Jacobian matrix, $\tilde{\mathbf{J}}_{n,k}$, same eigenvectors, $\tilde{\mathbf{e}}^m$, and same system coefficients, $\tilde{\alpha}^m$, for each layer. Consequently, the same eigenvalues, $\tilde{\lambda}^m$, defined as

$$\tilde{\lambda}^1 = \tilde{\mathbf{u}}\mathbf{n} - \tilde{c}; \quad \tilde{\lambda}^2 = \tilde{\mathbf{u}}\mathbf{n}; \quad \tilde{\lambda}^3 = \tilde{\mathbf{u}}\mathbf{n} + \tilde{c}, \tag{25}$$

where $\mathbf{u}$ is the velocity vector $\mathbf{u} = (u, v)$, and c refers to the wave celerity under shallow water assumption $c = \sqrt{gh}$. Note that the tilde variables account for the linearized values at the cell edges derived from Roe's linearization. A comprehensive detail of this procedure can be found in Ref. 23, and more discussion on the numerical fixes included in the model can be found in Refs. 22 and 40.

A. Computation of friction source terms

In shallow water models, the treatment of the friction source terms has been under study for years to find the most stable, robust, and efficient way to include it. The explicit inclusion of this term within the numerical contributions entails the existence of an additional stability condition that could govern and limit the time step size, Δt.[24–26] In order to avoid this global reductions of the time step, different numerical strategies have been proposed in the literature. On the one hand, the implicit introduction of these friction terms in a cell-centered manner has been used extensively.[27] This formulation, despite certain disadvantages such as not correctly preserving the steady states, provides good results and is very robust. Conversely, numerical fixes have been proposed in the context of upwind formulation that limit the source term strength instead of Δt,[22,23,38] allowing to keep the full explicit character of the scheme.

In this case, due to the sensitivity to the friction stresses between layers, specially when dealing with small oil depths over water, two options have been considered: on one side, a pure explicit approach, in which the interface friction participates in the upwind decomposition, has been implemented introducing a new contribution in $\tilde{\beta}$. The numerical fix proposed by Refs. 22 and 23 is applied only to bed friction. This numerical fix is based on physical constraints that cannot be applied straightforward to the interface between two fluids in the two-layer model.[23] For this reason, an alternative, based on a semi-implicit discretization of the interface friction source term, can be directly used within cell centers in the final updating expression for cases where numerical stability is more compromised.

Thus, the general expression for the update of conserved variables can be written in terms of both approaches as

$$\mathbf{U}_i^{n+1} = \mathbf{U}_i^n - \frac{\Delta t}{A_i}\sum_{k=1}^{N_E}\sum_{m=1}^{N_W}\left[\left(\tilde{\lambda}^- - \left(\tilde{\alpha} - \frac{\tilde{\beta}}{\tilde{\lambda}}\right)\tilde{\mathbf{e}}\right)^m_k l_k\right]^n + \vartheta \Delta t \mathbf{S}_{\tau w,i}, \tag{26}$$

where superscripts n and $n+1$ stand for the current and next time step, respectively, N_E refers to the number of neighbor elements of each cell, run with k up to 3 for the triangular mesh, N_W to the number of waves in the model, run with m up to 3 for each layer in the system (21), and ϑ is a switch that is equal to 1 when the semi-implicit centered discretization of the interface source term is chosen, and 0 if the explicit upwind discretization is used. The information is propagated according to the upwind philosophy: $\lambda^\pm = \frac{\lambda \pm |\lambda|}{2}$.

All the friction source terms can be evaluated at the shared wall, k, between two cells, projected onto the eigenvector basis and represented by means of an extra stationary wave using the so-called augmented Roe approach (ARoe approach).[22] They can contain not only information about topography and bed friction, but also friction terms of the two-layer system. The expression of source strengths, $\tilde{\mathbf{S}}_{\tau,k} = (\tilde{\beta}^1, \tilde{\beta}^2, \tilde{\beta}^3)^T_k$, contains additional terms as

$$\tilde{\beta}^1 = -\frac{1}{2\tilde{c}}\left(\delta\mathcal{Z}_b + \frac{\tilde{\tau}_{a,n}}{\rho} + (1-\vartheta)\frac{\tilde{\tau}_{w,n}}{\rho} + \frac{\tilde{\tau}_{b,n}}{\rho}\right), \quad \tilde{\beta}^2 = 0, \quad \tilde{\beta}^3 = -\tilde{\beta}^1, \tag{27}$$

where $\tilde{\tau}_{,n}$ accounts for the discretized and projected friction stresses. For this model, where dynamics is extremely sensitive to friction terms, the projection has been made not over the normal of the cell edge, as in the single layer model, following,[22] but over the velocity direction, which provides better results when friction governs.[41] Therefore, the bottom stresses are given as follows:

$$\tilde{\tau}_{b,n} = \frac{\tilde{n}_b^2\, \tilde{\mathbf{u}} \cdot \mathbf{n_{uL}} \min(|u_i|, |u_j|)}{\max(h_i, h_j)^{4/3}} d_n, \tag{28}$$

with $\tilde{n}_b = \frac{1}{2}(n_i + n_j)$ being the averaged Manning's coefficient between cells, d_n the normal distance between the cell centers, and $\tilde{\mathbf{u}} \cdot \mathbf{n_{uL}} = \tilde{u}\, n_{ux} + \tilde{v}\, n_{uy}$ the average states at each wall k represented with the tilde variables.

The friction between fluid and wind (air)[10–12] is

$$\tilde{\tau}_{a,n} = \rho_a C_a \tilde{\mathbf{u}} \mathbf{n_{ur,a}} \min(|u_i|, |u_j|) \frac{d_n}{\rho}; \tag{29}$$

1. Explicit upwind approach for source terms

In particular, when the explicit upwind approach is also used for friction between layers ($\vartheta = 0$), the augmented approach includes in

the source term strengths, $\tilde{\beta}$, all the stresses of the problem: bed friction modeled as in (28), air friction following (29), and interface friction modeled with a Chezy formula[42] as

$$\tilde{\tau}_{w,n} = \rho g C_f \tilde{\mathbf{u}}\mathbf{n}_{\mathbf{ur,w}} \min(|u_i|, |u_j|) \frac{d_n}{\rho}, \tag{30}$$

where normal vectors are computed with velocities using Eqs. (6)–(8).

2. Semi-implicit computation of the shear stress between layers

If contributions of interface friction are subtracted from source strengths and discretized cell centered, source strengths only contain the bed and air contributions and interface friction is used for updating the final conserved variables, as seen in (26) with $\vartheta = 1$.

In that case, the centered discretized source term for the layer $L = 1$ (upper layer) is

$$\mathbf{S}_{\tau w,i} = -gCf \left| \frac{(hu)_1}{h_1} - \frac{(hu)_2}{h_2} \right|_i^n \left(\frac{(hu)_1^{n+1}}{h_1^n} - \frac{(hu)_2^n}{h_2^n} \right)_i, \tag{31}$$

which is introduced into the momentum equation of system (26), to get the final updating for the discharge, $h_L u_L$. The state $n+1$ at layers is obtained as a function of its intermediate state *, obtained from upwind contributions and wave strengths in (26), and the semi-implicit term. Thus, the approach yields for a generic layer, L, as

$$\begin{aligned} (hu)_L^{n+1} &= \frac{(hu)_L^* + \Delta t C_{f1} g \dfrac{(hu)_2^n}{h_2^n} |u_{r,w}|^n}{1 + \Delta t C_{f1} g \dfrac{1}{h_L^n} |u_{r,w}|^n}; \\ (hv)_L^{n+1} &= \frac{(hv)_L^* + \Delta t C_{f1} g \dfrac{(hv)_2^n}{h_2^n} |v_{r,w}|^n}{1 + \Delta t C_{f1} g \dfrac{1}{h_L^n} |v_{r,w}|^n}, \end{aligned} \tag{32}$$

with $u_{r,w}$ and $v_{r,w}$ the x and y components of the relative velocity between layers. As these source terms are discretized implicitly and cell centered, they only affect x and y momentum.

B. Computational algorithm and model

The model is designed so that by providing initial conditions for the variables (level, oil temperature if present, and velocity field) and boundary conditions that provide information on how the flows enter and exit the physical boundaries of the domain, the model progresses over time providing information on the transient evolution of the oil layer above the water and/or land layer, in terms of draught, velocities, and temperatures.

For that purpose, each time step that the simulation runs forward, this methodology solves both layers as a coupled model. It starts from an initial condition of conserved variables for each layer (h_L, $h_L u_L$, and $h_L v_L$) and computes all the numerical contributions, which are a consequence of inner waves and boundary condition perturbations. With those contributions, the conserved variables can be updated and, consequently, also the secondary variables (u_L, v_L, $z_{b,1}$) and oil layer features (T_1, ρ_1) can be computed.

When dealing with the global model in a synchronous form, one of the issues concerns the global time step size. Conversely, an algorithm to distinguish the proper friction terms which apply to each layer, depending on the situation, is also required. In Fig. 2, a general flow chart of the global algorithm is represented. Additionally, some details are described next.

On one side, for each layer L, the time step size, Δt_L, is dynamically computed, limited by the CFL condition: $CFL \in (0, 1)$,[43] and responds to the dynamics of the layer following

$$\Delta t_L = \mathrm{CFL} \left(\min_{k,m} \frac{\delta x_k}{\tilde{\lambda}_k^m} \right)_L, \tag{33}$$

where

$$\delta x_k = \min(\chi_i, \chi_j) \quad \chi_i = \frac{A_i}{\max\limits_{k=1,NE} l_k}, \tag{34}$$

recalling that l_k stands for the cell edge length, while A_i is the cell area.

However, in the context of a two-layer model, both layers must be explicitly updated with the same time step size. For this reason, a normalization of the time step must be done, so that the global time step size is

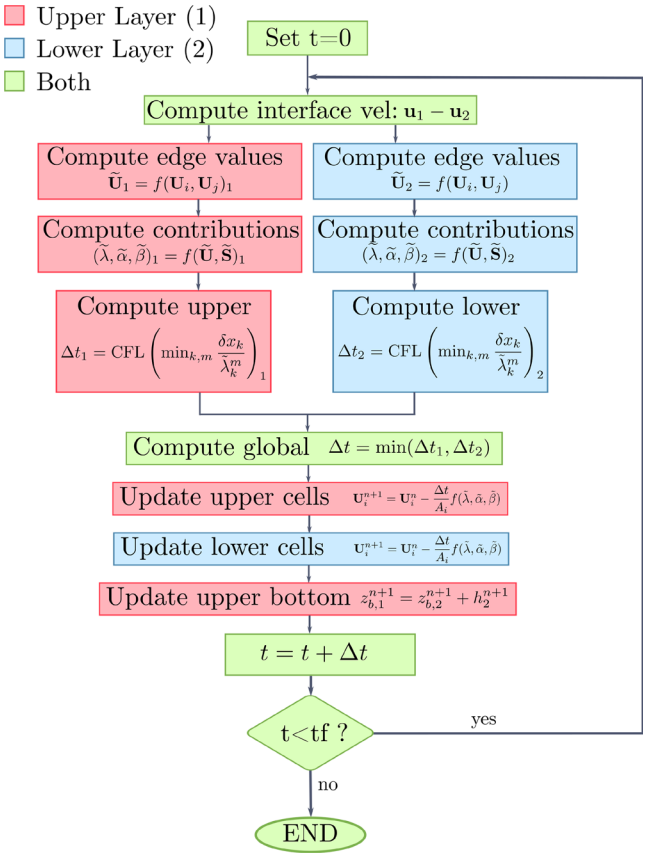

FIG. 2. Sketch of the algorithm flow chart.

$$\Delta t = \min(\Delta t_1, \Delta t_2), \tag{35}$$

with Δt_1 and Δt_2 the upper and lower layer minimum time step size, respectively.

Regardless of the discretization approach chosen for the interface stress contribution, the general friction source term has three components $\mathbf{S}_\tau(\mathbf{U}) = \mathbf{S}_{\tau a}(\mathbf{U}) + \mathbf{S}_{\tau w}(\mathbf{U}) + \mathbf{S}_{\tau b}(\mathbf{U})$, that cannot be acting at the same time over a layer, as it would be unphysical. The following cases, represented in Fig. 3, are identified:

1. If both layers are wet ($h_1 > 0$ and $h_2 > 0$):
   - The wind stress, $\mathbf{S}_{\tau a}(\mathbf{U})$, acts over layer 1;
   - The interface stress, $\mathbf{S}_{\tau w}(\mathbf{U})$, acts over both layers 1 and 2;
   - Bed stress, $\mathbf{S}_{\tau b}(\mathbf{U})$, acts over layer 2.
2. If the oil upper layer is dry ($h_1 = 0$ and $h_2 > 0$):
   - The wind stress, $\mathbf{S}_{\tau a}(\mathbf{U})$, acts over layer 2;
   - Interface stress, $\mathbf{S}_{\tau w}(\mathbf{U})$, is not acting;
   - The bed stress, $\mathbf{S}_{\tau b}(\mathbf{U})$, acts over layer 2.
3. If the lower layer is dry ($h_1 > 0$ and $h_2 = 0$):
   - The wind stress, $\mathbf{S}_{\tau a}(\mathbf{U})$, acts over layer 1;
   - The interface stress, $\mathbf{S}_{\tau w}(\mathbf{U})$, is not acting;
   - The bed stress, $\mathbf{S}_{\tau b}(\mathbf{U})$, acts over layer 1.

Here, one of the main advantages of this two-layer model arises. As an alternative to traditional particle tracking oil spill models, the model presented here allows the oil layer evolution as a fluid layer, even in cases where water does not exist. This situation can happen when oil spills arrive to coastal areas and reach the land and also when oil pipes fail inland and spills are produced overland close to coastal areas, which could reach the sea eventually.

C. Computation of age and temperature transport

Both oil age, a, and temperature, T, evolution are scalar transport equations. They can be computed decoupled from the hydrodynamic finite volume scheme [i.e., Eq. (26)], being updated with the previously computed velocity field. Following Ref. 44, the analysis of the augmented Riemann solver allows to define a numerical flux, $(hu_{\boldsymbol{n}})_k^{\downarrow}$, that decouples the transport system from the hydrodynamics preserving conservation. Defining a general transported value, ϕ, the numerical flux at each edge, k, between cells i and j is

$$(hu_{\boldsymbol{n}})_k^{\downarrow} = (hu_{\boldsymbol{n}})_i + \sum_{m=1}^{3} \left(\tilde{\lambda}^{-} \tilde{\gamma} \tilde{\mathbf{e}}_1\right)_k^m, \tag{36}$$

with $(hu_{\boldsymbol{n}})_k$ the projection of the discharge over the normal vector from cell i to j, $\mathbf{n} = (n_x, n_y)$, defined as $(hu_{\boldsymbol{n}})_k = (h\mathbf{un})$, where $\mathbf{u} = (u, v)$. Taking into account this definition, the updating expression for an arbitrary transported scalar, ϕ, is

$$(h\phi)_i^* = (h\phi)_i^n - \frac{\Delta t}{A_i} \sum_{k=1}^{N_E} (hu_{\boldsymbol{n}}\phi)_k^{\downarrow} l_k, \tag{37}$$

where

$$\phi_k^{\downarrow} = \begin{cases} \phi_i & \text{if} \quad (hu_{\boldsymbol{n}})_k^{\downarrow} > 0 \\ \phi_j & \text{if} \quad (hu_{\boldsymbol{n}})_k^{\downarrow} < 0. \end{cases} \tag{38}$$

Note that this notation is common for any scalar, ϕ, such as T or a. Their final update depends on the source term, which is computed cell-centered in both cases as follows:

$$(h\phi)_i^{n+1} = (h\phi)_i^* + \Delta t \mathcal{S}_{\phi,i}, \tag{39}$$

where $\mathcal{S}_\phi$ is the source term. In the case of the temperature equation, $\mathcal{S}_{\phi,i}$ is the discretized version of $\mathcal{S}_\mathcal{T}$, defined in Eq. (14). The discrete values of variables for the upper layer when available as

$$\mathcal{S}_{\mathcal{T},i} = \frac{1}{\rho_i C_p} \left[\dot{Q}_{rad} + h_{c,a,i}(T_i - T_{air}) + h_{c,w,i}(T_i - T_{water})\right] \tag{40}$$

are used, defining $h_{c,a,i}$ and $h_{c,w,i}$ as in (16a).

In the case of oil age, the source term, $\mathcal{X}_c$, coming from Eq. (20) is just a discrete distribution of 0 or 1, depending on the oil depth.

D. Computation of oil evaporation

Once the *age* and T have been computed and updated for each cell of the computational domain, the evaporation can be computed in order to update the source term of mass equation (4a) of the upper layer.

In general terms, the evaporation rate is obtained as

$$f_{evap,i} = \frac{F_{v,i} - F_{v,old,i}}{\Delta t} h_i, \tag{41}$$

after computing the new evaporation fraction, $F_{v,i}$, at each cell following Eq. (19).

When the evaporation rate or evaporation velocity, f_{evap}, has been computed, the water depth can be updated at each cell as

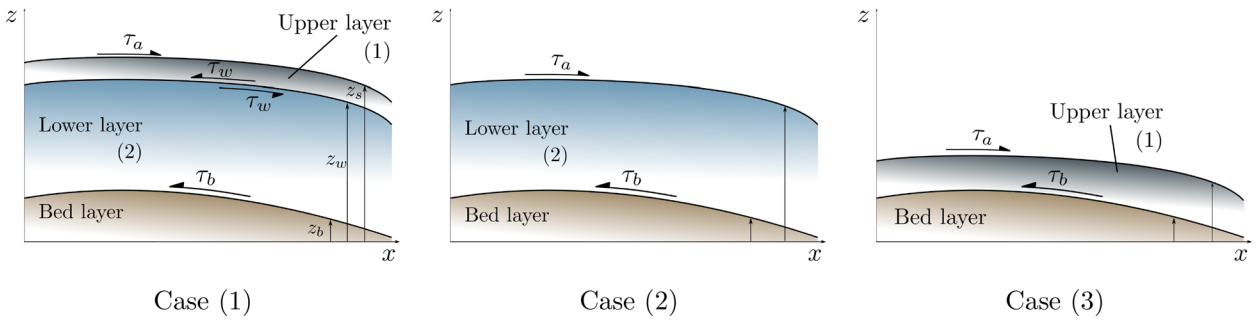

FIG. 3. Representation of friction stresses acting over each layer in the different identified cases.

$$h^{n+1} = h^* - \theta f_{evap,i}\Delta t, \tag{42}$$

where h^* represents the value of water depth already updated with computational fluxes from the homogeneous part of the equation. Remember that θ is equal to 1 in the upper layer. Thus, evaporation update is only performed in the oil layer. Finally, note that the evaporation rate needs to be truncated in the case of not having enough mass in the cell to evaporate all. This is, if $f_{evap,i}\Delta t > h^*$, then h^{n+1} is set to 0 (dry cell).

IV. OIL SPILLS TWO-LAYER MODEL VALIDATION AND APPLICATIONS

A. Steady state validation with reference solution

The two-layer SW system can be validated for steady states by assuming 1D flow, removing temporal derivatives and assuming a constant discharge in both layers. MacDonald proposed different reference solutions for a one-layer model in 1D,[45] and this idea can be extended to a generic two-layer model.[19] In this work, this idea has been applied to the two-layer model assuming the thin layer hypothesis and including the wind as an additional stress in the upper layer, getting

$$\frac{d(q_1)}{dx} = 0, \tag{43a}$$

$$\frac{dh_1}{dx}\left(1 - Fr_1^2\right) = \left(\frac{dz_b}{dx} + \frac{dh_2}{dx}\right) - \frac{\tau_w}{gh_1\rho_1} + \frac{\tau_a}{\rho_2 h_1 g}, \tag{43b}$$

$$\frac{d(q_2)}{dx} = 0, \tag{43c}$$

$$\frac{dh_2}{dx}\left(1 - Fr_2^2\right) = -\left(\frac{dz_b}{dx}\right) + \frac{\tau_w}{gh_2\rho_2} - \frac{\tau_b}{gh_2\rho_2}, \tag{43d}$$

where Fr_L stands for the Froude number, computed as u/c, with c the celerity of the system $c = \sqrt{gh}$. The variables q_1 and q_2 represent the unit discharge at each layer, which does not vary in space. Re-ordering system (43), the equations can be written in terms of the distribution of the two unknowns, $h_2(x)$ and $z_b(x)$, if $h_1(x)$ is given as input,

$$\frac{dh_2}{dx} = \left(-\frac{gh_2^3}{q_2^2}\right)\left[\frac{dh_1}{dx}\left(1 - \frac{q_1^2}{gh_1^3}\right) + C_f(u_1 - u_2)|u_1 - u_2|\left(\frac{1}{h_1} + \frac{r}{h_2}\right) + \frac{\tau_a}{\rho_1 h_1 g} - \frac{n_b^2 u_2|u_2|}{h_2^{4/3}}\right], \tag{44a}$$

$$\frac{dz_b}{dx} = -\left[\frac{dh_2}{dx}\left(1 - \frac{q_2^2}{gh_2^3}\right) - r\frac{c_f}{h_2}\left(\frac{q_1}{h_1} - \frac{q_2}{h_2}\right)\left|\frac{q_1}{h_1} - \frac{q_2}{h_2}\right| + \frac{n_b^2 u_2|u_2|}{h_2^{4/3}}\right]. \tag{44b}$$

This resulting system, although is still lacking of analytical solution, can be easily computed by using an ODE-solver (i.e., Python function *odeint* from SciPy library). After providing a spatial distribution of the upper layer depth and both constant discharges as input, the lower layer depth and bottom are provided as a result by the solver. Additionally, some other values are needed to define the solution: boundary conditions at bottom elevation, $z_b(0)$, and lower layer, $h_2(0)$, functions (at x = 0 m), density of both layers, and friction parameters. In Table I, all the chosen parameters set in the ODE-solver to solve system (43) are summarized.

In order to perform this validation, the above-mentioned reference solution is compared with the solution along a channel of fixed width simulated with the 2D model. Two different steady cases, case A, frictionless, and case B, with friction, have been computed. The inflow boundary condition ($x = 0$ m) is a constant discharge at each layer, while the outflow boundary condition ($x = 150$ m) is a constant fluid level. Both simulations begin with initial conditions corresponding to uniform surface elevation and zero velocity in the whole domain. In both cases, the upper layer depth distribution follows

$$h_1(x) = c + d\exp\left[-b\left(\frac{x}{150 - a}\right)^2\right], \tag{45}$$

where a = 0.5, b = 33.75, c = 0.8, and d = 0.25, and the function is bounded $h_1(x) \in [0, L]$, with $L = 150$ m. These values have been selected as an adaptation of those found in the literature to the thin two-layer model.[19,45]

The steady states are simulated with the 2D two-layer model, mapped over a line along the x axis and compared with the reference solutions. The numerical simulations are carried out over an unstructured triangular mesh with 4913 computational elements, whose area ranges from the 0.5 to 0.14 m^2 in the smallest cells. This mesh, as well as all those built for this work, has been done with Triangle.[46] The topography represents a 10 m transversal extension of the bed distribution provided by the reference solution, as seen in Fig. 4, where the mesh and the surface layers at final state are represented in 3D.

The constant discharge corresponding to the steady solution is set at each layer as the inflow boundary condition, while the constant fluid level at the outflow boundary is imposed at the outlet condition. Both numerical simulations are carried out starting with an initial condition given by a constant fluid level determined by the inlet boundary condition (at x = 0 m). A transitory simulation is developed until 2000 s, to ensure that the flow converges to the steady state. The simulations are carried out using CFL = 0.95.

Figures 5 and 6 show the comparison between the numerical results with a 2D unstructured mesh and the 1D reference solution in case A and B, respectively. In both figures, the left plot represents the bottom and layers' surface elevation, while the right plot shows the x velocity distribution.

TABLE I. Parameters to define reference steady solutions.

	ρ_1	ρ_2	ρ_a	q_1	q_2	$z_b(0)$	$h_2(0)$	C_f	n_b	U_a	C_a
Case A	1.0	3.0	1.29×10^{-3}	1.0	0.4	0.5	1.5	0.0	0.0	0.0	0.0
Case B	1.0	3.0	1.29×10^{-3}	1.0	2.0	1.5	0.4	0.01	0.04	40.0	0.005

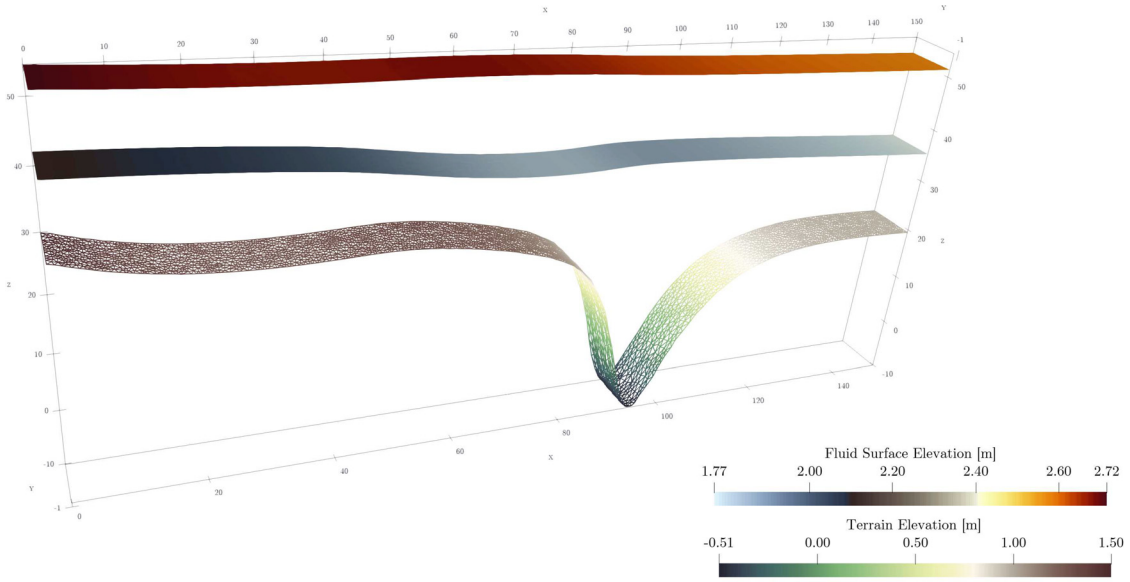

FIG. 4. 3D representation of the layers surface elevation and computational mesh in the bottom for the steady state (case B) simulated with the 2D two-layer model.

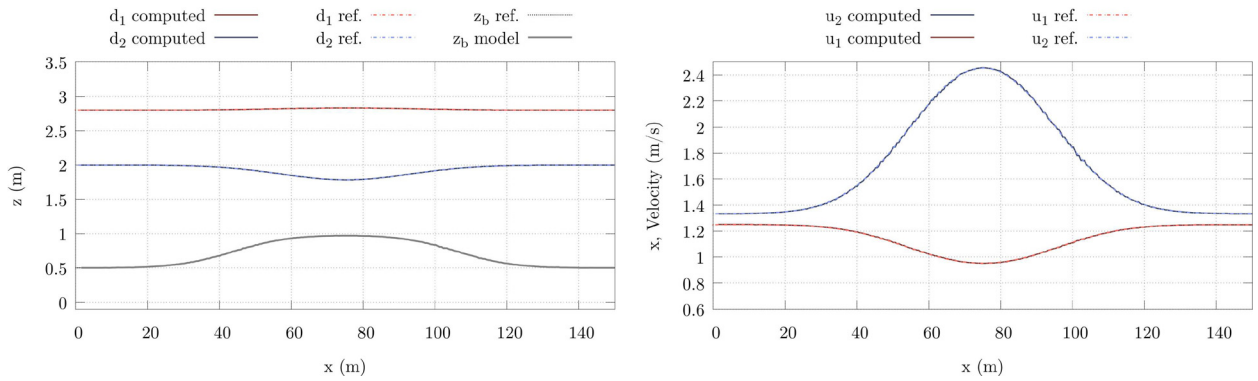

FIG. 5. Comparison between the numerical results with a 2D unstructured mesh and the 1D reference solution for the two-layer steady state in case A (without friction) in terms of surface elevation (left) and velocity (right).

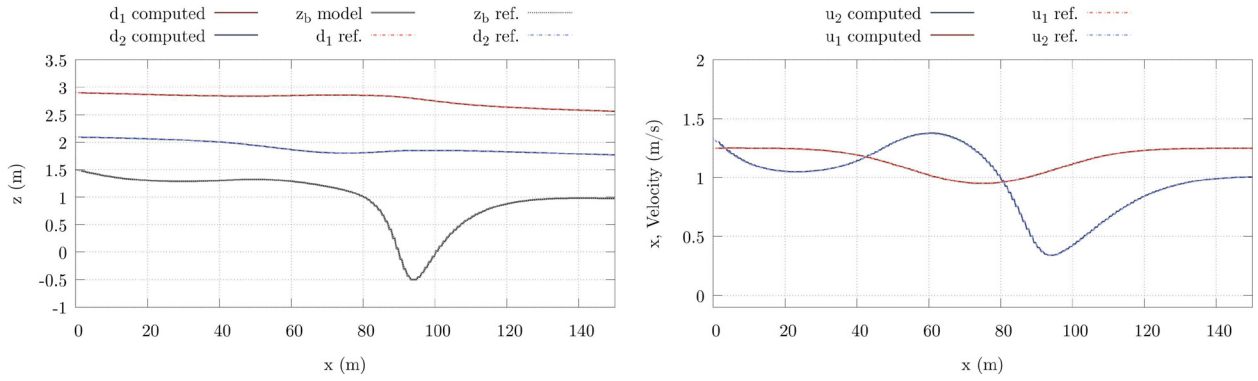

FIG. 6. Comparison between the numerical results with a 2D unstructured mesh and the 1D reference solution for the two-layer steady state in case B (with friction) in terms of surface elevation (left) and velocity (right).

B. Validation of the evaporation rate numerical performance in an academic test case

In order to validate the mass conservation during the evaporation process in the model and the performance of the evaporation model chosen, a test case is carried out focusing on the mass evolution in the upper layer. A squared domain of side length 10 km is considered. Both layers cover the whole domain and are initially at rest, surrounded by closed boundaries. The initial water depth at the lower layer is 1 m, while the upper layer has an oil depth of 0.1 m. Therefore, there are 10×10^6 cubic meters of oil initially.

The model provided by Ref. 18 is used with a maximum evaporation rate $\mathcal{E}_{\max}$ corresponding to the 5% of the available mass ($\mathcal{E}_{\max} = 0.05$), whose value is based on observations. Although this is a proper value for the simulation of realistic cases, in this test case in which the purpose is to understand the model behavior, the maximum evaporation has been increased to 50%, that is, $\mathcal{E}_{\max} = 0.5$. Additionally, this maximum can be activated or deactivated to analyze the effect on the results.

Different test cases have been carried out, and their characteristics are summarized in Table II. The heat transfer is null in all the cases except in case 2 and 2L, where a positive heat transfer is considered so the temperature of the oil slick increases up to 19.96 and 17.62 °C, respectively. The parameters to compute the heat flux source term [see Eq. (14)] in cases 2 and 2L are 10° (283.15 K) for water temperature and 45° (318.15 K) for air temperature; $\dot{Q}_{rad} = 1000$ W/m^2 for solar radiation, $c_p = 1900$ W/m^2, as specific oil heat and null wind velocity.

The maximum temperature reached by the oil layer can be seen in column T_{max}, which is the oil temperature at the end of the simulation. This temperature differs from the initial condition only in cases 2 and 2L, where external heat flux source term is activated. The initial temperature of the oil slick is set to 15 °C in cases 1, 1L, 2, and 2L, while the initial temperature of cases 3 and 3L is the same as the final temperature reached by cases 2 and 2L. In Fig. 7, the unstructured mesh with 5124 triangular cells used for the test case can be seen. The CFL is set to 0.95 and the simulations run during 200 s.

In Fig. 8, the time evolution of the oil volume within the domain, V_l, is represented together with the evaporated volume, V_E. In the same figure, the total mass (i.e., their sum) is represented, so that the constant initial value is preserved to machine precision.

All the cases preserve the total amount of mass, validating the evaporation physical model. Additionally, this test case highlights the effects of evaporation limit, temperature, and heat transfer not only in the total evaporated mass, but also in the evaporation velocity.

TABLE II. Summary of numerical test cases performed for the validation of the evaporation rate model.

Case	T_{ini} (°C)	$\dot{Q}$	$\mathcal{E}_{\max}$	$T_{\max}$ (°C)
Case 1	15.00	0	∞	15.00
Case 1L	15.00	0	0.5	15.00
Case 2	15.00	>0	∞	19.96
Case 2L	15.00	>0	0.5	17.62
Case 3	19.96	>0	∞	19.96
Case 3L	17.62	>0	0.5	17.62

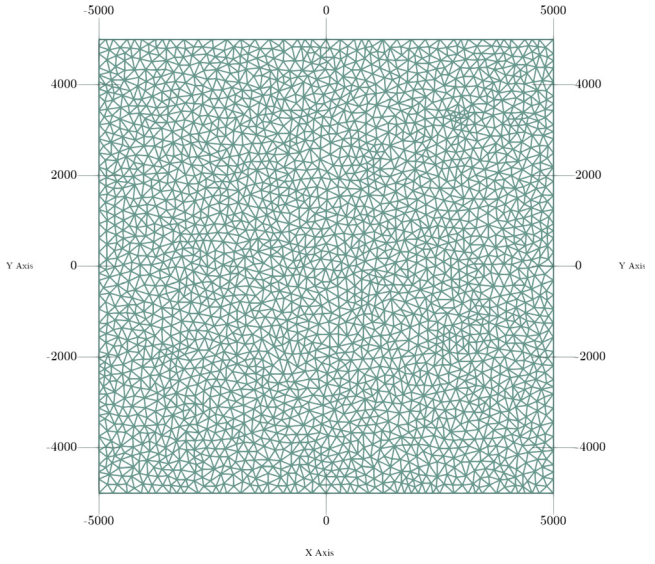

FIG. 7. Wireframe of the unstructured computational mesh used to discretize the 2D domain in the evaporation test case.

First, the comparison of the total mass with and without limit seen in Fig. 8 shows the threshold effect of $\mathcal{E}_{max}$. It is worth noting that it acts as a limit each time step limiting the percentage of mass (i.e., oil depth) that can be evaporated at time t and cell i. Thus, when it is set to 50%, as in this case, the total evaporated mass reaches a bit less than the 40% of the total mass.

In Fig. 9, the same results of cases 1 and 1L are compared with those starting with the same temperature but with the heat transfer mechanism active (cases 2 and 2L). In Fig. 9(a), the evolution of mass without limits can be seen, while (b) plots the results with $\mathcal{E}_{\max}$ limiting. It is worth recalling that the temperature increase affects the evaporation velocity, but the final evaporation mass will be different only in the case of not having an evaporation limit. All results are plotted in the same graph and can be seen in Fig. 10 for proper comparison.

Finally, as evaporation also depends on oil age (which in this case coincides directly with time), simulations in which the initial temperature is as high as reached by cases 2 and 2 L are carried out. The results are shown in graphs (a) and (b) of Fig. 11. In both cases, regardless of

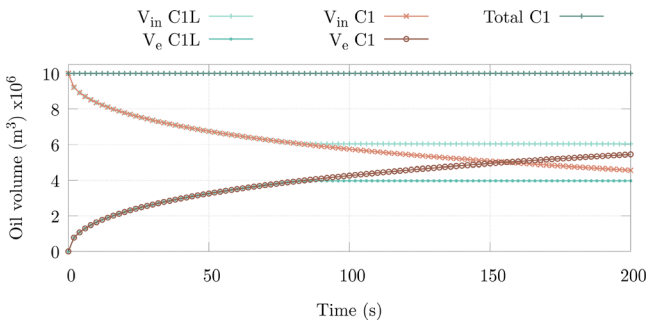

FIG. 8. Evolution of oil volume inside the domain, V_l, evaporated volume, V_E, and total mass ($V_l + V_E$) for cases 1L and 1L.

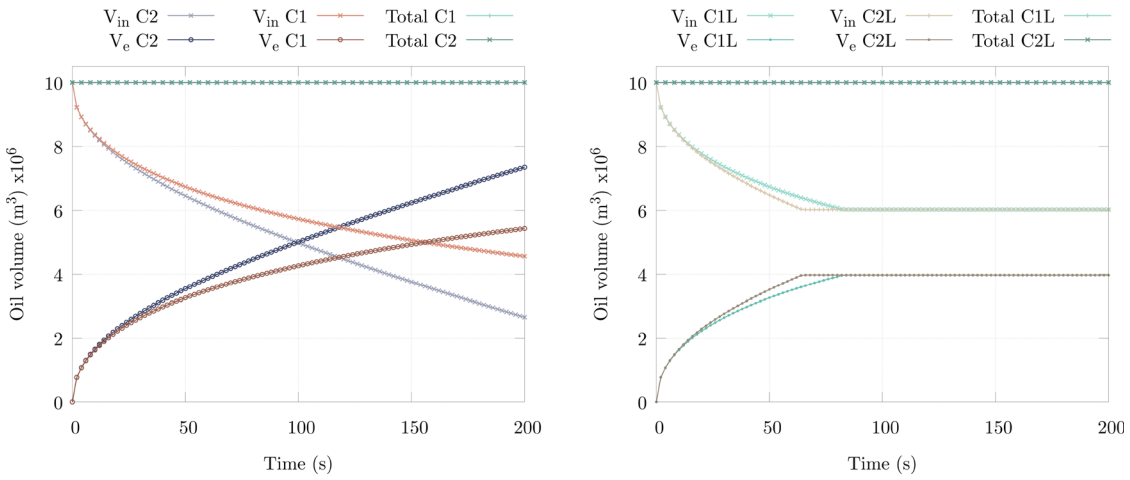

FIG. 9. Divided comparison between cases 1 and 2 (a) and 1L and 2L (b) of the oil volume evolution inside the domain, V_I, evaporated volume, V_E, and total mass ($V_I + V_E$).

the use of the evaporation limit, the evaporation velocity increases significantly for higher temperatures, even the age of oil during first stages of the simulation is not as high.

C. Test case for friction discretization assessment

The aim of this test case is to assess and compare two different friction treatments, explicit upwind and semi-implicit centered, in the two-layer model. The test case focuses on understanding the impact of these two approximations on extreme situations such as those corresponding to irregular topography and wet-dry fronts with variable bottom and strong friction terms. The 2D simulation results are analyzed, particularly in terms of water surface elevation, velocity fields, flow patterns, and wet-dry treatment. Additionally, the mesh convergence of the model with and without friction, which is another important numerical aspect of the scheme, is also addressed.

For all the analysis performed, the simulation domain is a square, $10.0 \times 10.0\,\mathrm{km}^2$. It has closed boundaries and a Gaussian mound in the middle of the domain representing a variable bottom that reaches a total height of $z_b = 10.0$ m, starting from $z_b = 0$ m. Initially, the oil layer has a constant level of 7.0 m, and the lower water layer has an initial discontinuity along one of the boundaries, which varies from 6.0 to 4.5 m, that will cause a wave in both layers moving around the island. The longitudinal profile and its 3D representation can be seen in Figs. 12 and 13, respectively.

In this case, there is no wind stress $\tau_a = 0$, the Manning roughness coefficient at the bottom is $n = 0.032$ and the Chezy coefficient between layers is $C = 0.01$, which corresponds to a high value.

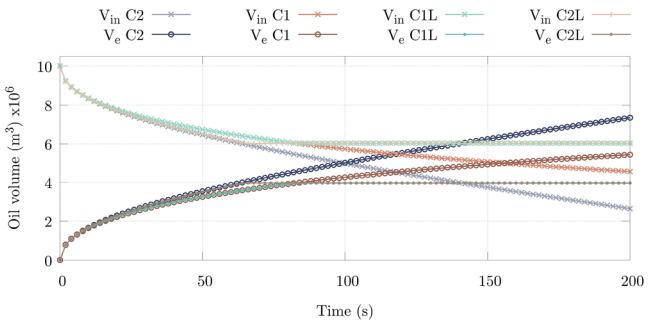

FIG. 10. Comparison between cases 1 and 2 of oil volume evolution inside the domain, V_I, and evaporated volume, V_E, without and with evaporation limit.

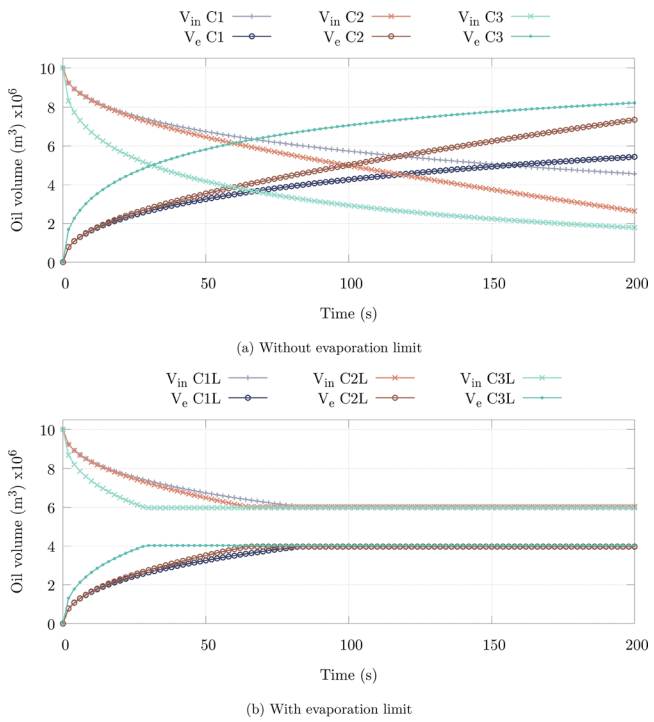

FIG. 11. Comparison between cases 1, 2, and 3 of the oil evaporation evolution without limit (a) and 1L, 2L, and 3L with evaporation limit (b).

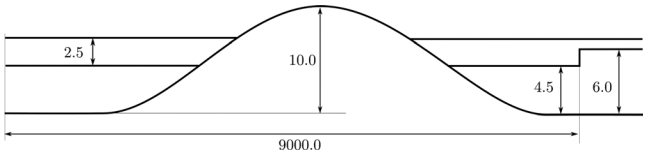

FIG. 12. Sketch of the initial condition profile representing the surface level and bottom of both layers for the friction assessment test case.

The upper density is assumed constant $\rho_1 = 800\,\mathrm{kg/m^3}$ as well as in the lower layer $\rho_2 = 1000\,\mathrm{kg/m^3}$.

1. Friction discretization assessment

For the simulation for friction discretization comparison, the total time is 5000.0 s and CFL = 0.9 is used. The domain is discretized over an unstructured triangular coarse mesh, named M1 (mesh 1), containing 5124 computational elements, generated setting a maximum cell size of $32\,000\,\mathrm{m^2}$ in the Triangle mesher.[46] Three different cases are considered for comparison: explicit case, with a full explicit formulation of all the friction terms; semi-implicit case, with an augmented Roe approach for bottom friction but a semi-implicit discretization for interface friction; and a slip case, without friction between layers, just for comparison purposes.

In Figs. 14 and 15, the 2D spatial distribution of fluid depth can be seen for both layers at different times. The initial condition is the same for the three cases in both layers. In Fig. 14, the same distribution is presented at $t = 400$ s. It can be seen that the order of magnitude is almost the same in both the explicit and the implicit discretization, although the explicit one shows an erratic wave advance, while the implicit one shows a smoother solution. Both solutions can be compared with the frictionless case, which presents a very different distribution. In Fig. 15, the 2D distribution is shown again for both layers at $t = 750$ s. At this stage, it is possible to see how some instabilities appear close to the wet/dry front in the upper layer of the explicit discretization (a), while the implicit approach presents a smooth pattern. Nevertheless, these two discretizations show a very different pattern from those of the frictionless simulation, which is propagated with less diffusion.

Additionally, in Fig. 16, the 2D velocity field of the upper layer is shown over its water depth 2D distribution, which is only plotted when depth is not null. The velocity fields show how the frictionless case is much more accelerated than the ones with friction, which present a very similar behavior. However, the main difference between these two discretizations is the instabilities that appear in the explicit discretization, not present in the implicit approach.

In order to ensure stability, a last approach is implemented to achieve positive water depths. This approach halves the time step size if at least one cell with negative depth is detected. Although the final time of the simulation is 5000 s, the most evolved results shown only reach $t = 750$ s. The reason is due to the explicit discretization, which needs to use this safety approach around that time or the time step reduces almost to zero, turning the simulation into unaffordable. In Fig. 17, the time evolution of time step, Δt, can be seen and the behavior of the halving approach is registered.

2. Mesh convergence analysis

Over the same domain, a mesh convergence analysis is performed to ensure that the results do not vary while refining the computational mesh and, thus, can be considered stable and reliable. The analysis starts with previous coarse mesh, M1, and the maximum size of cells is halved seven times generating seven different meshes, whose characteristics are summarized in Table III. The total time of the simulation is 400.0 s, and CFL = 0.9 is used. From the three friction previous cases, two of them have been selected for comparison: the semi-implicit and the frictionless case.

As there is no analytical solution to compare with, the mesh convergence analysis is performed comparing between meshes and computing the root mean square error (RMSE). Additionally, as the simulation is performed over unstructured meshes that vary with the refinement, the results are mapped over a profile with a constant number of points, N_p, acting as probes for comparison between meshes. The profile is located in the middle point of the domain in order to get wet/dry fronts for checking purposes. In particular, it is discretized in

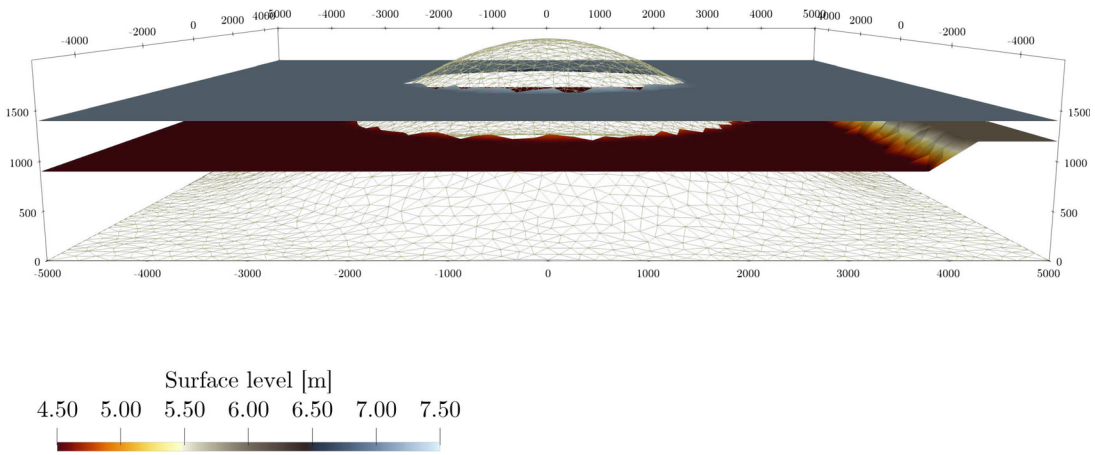

FIG. 13. 3D representation of the initial condition representing the surface level and bottom of both layers for the friction assessment.

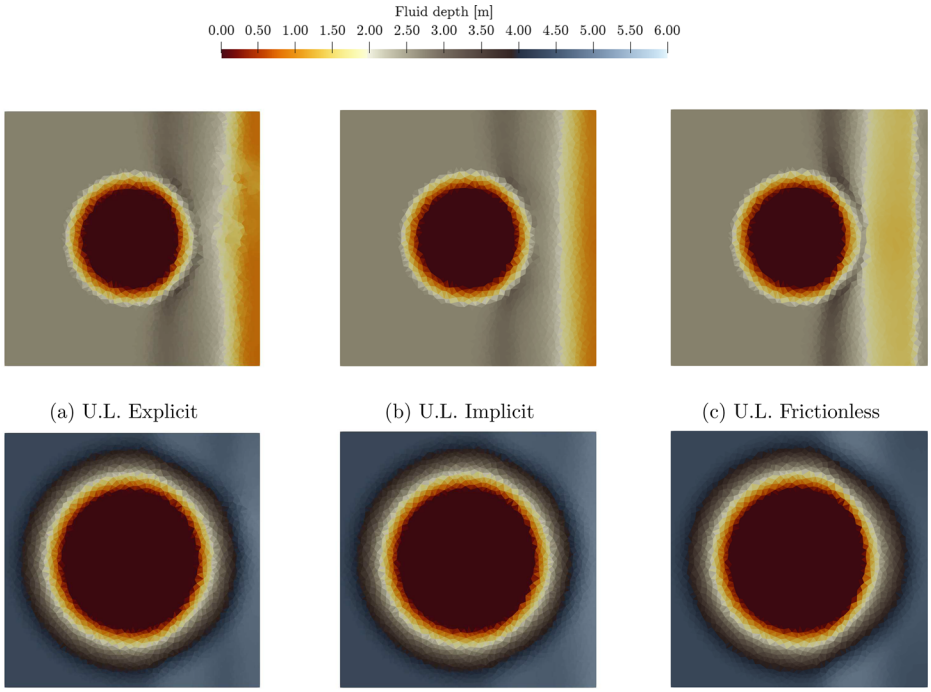

FIG. 14. 2D spatial distribution of fluid depth in the upper layer at $t = 400$ s for explicit (a), implicit (b), and frictionless (c) cases; and for lower layer with explicit (d), implicit (e), and frictionless (f) cases.

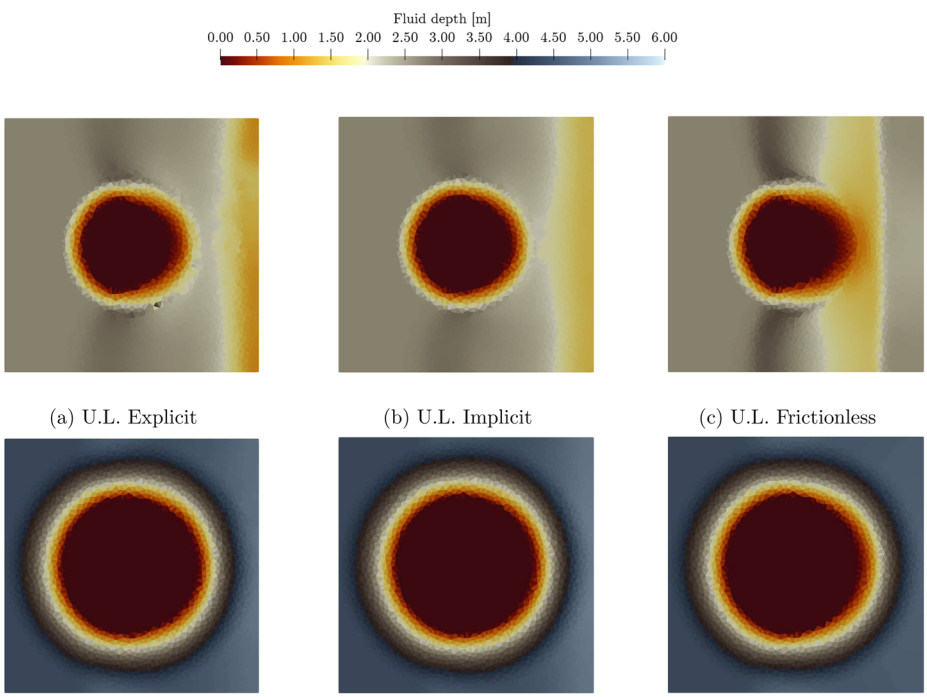

FIG. 15. 2D spatial distribution of fluid depth in the upper layer at $t = 750$ s for explicit (a), implicit (b), and frictionless (c) cases; and for lower layer with explicit (d), implicit (e), and frictionless (f) cases.

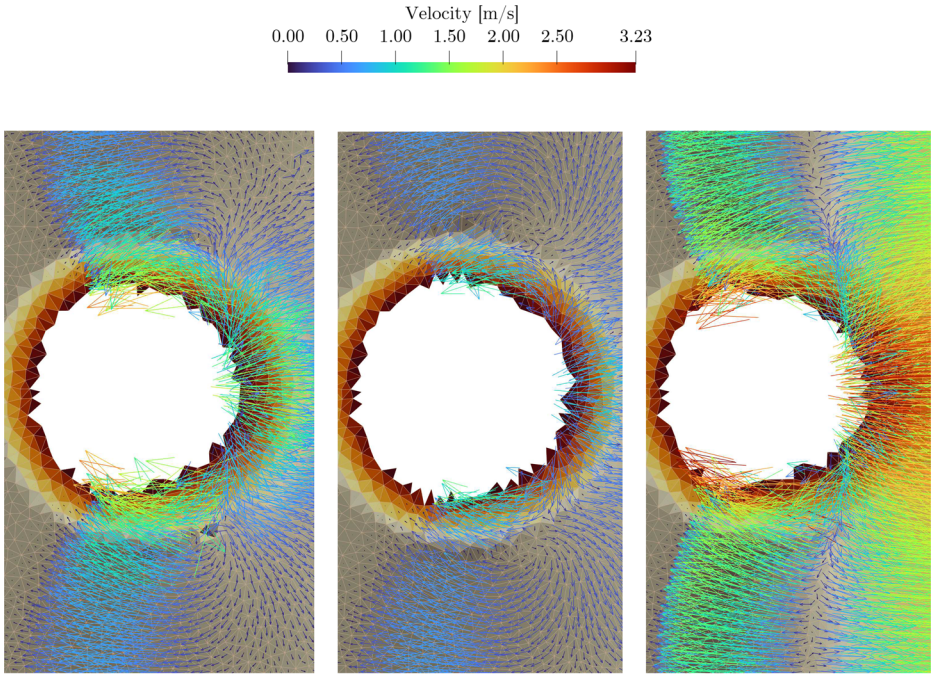

FIG. 16. 2D velocity in the upper layer at $t = 750$ s for explicit (a), implicit (b), and frictionless (c) cases.

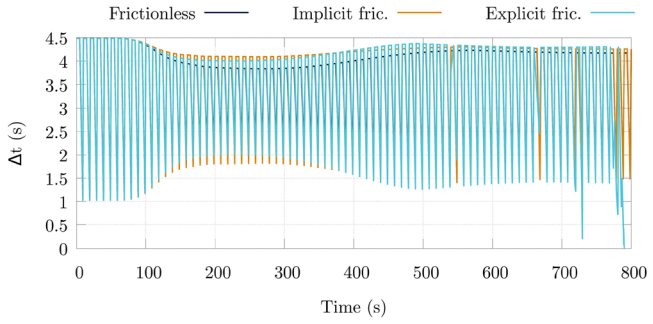

FIG. 17. Evolution of the time step, Δt, for each case in the friction discretization assessment.

TABLE III. Geometric characteristics of computational meshes used for the mesh convergence analysis.

Mesh	Max. cell area (m^2)	Number of cells
M1	32 000	5 124
M2	18 000	10 205
M3	8 000	20 481
M4	4 000	40 857
M5	2 000	81 761
M6	1 000	163 501
M7	500	327 242

100 000 points covering the line that goes from point (−5000.0, 0.0) to point (5000.0, 0.0). The RMSE is computed as

$$RMSE_{M_aM_b} = \frac{1}{N_p}\sqrt{\sum_{p=0}^{N_p}\left[h_{p,a}(t^n) - h_{p,b}(t^n)\right]^2}, \tag{46}$$

where a and b represent two consecutive meshes, and the summation runs through all points, p, of the profile computing the difference between the water depth of *mesh a* and *mesh b*. This comparison is done at a specific time $t^n = 400.0$ s, as it is sufficiently advanced for the dam break wave to have reached the dry/wet boundary caused by the existence of the bottom bump. In Table IV, all the computed RMSE between meshes for both friction cases are summarized. For both cases, the RMSE decreases up to small values, indicating that the results are getting similar when refining.

TABLE IV. RMSE of water depth between different meshes for the semi-implicit and the frictionless cases.

Compared meshes	Semi-implicit friction	Frictionless
$RMSE_{M1M2}$	0.076 068	0.070 861
$RMSE_{M2M3}$	0.054 392	0.058 249
$RMSE_{M3M4}$	0.038 365	0.051 610
$RMSE_{M4M5}$	0.021 936	0.035 712
$RMSE_{M5M6}$	0.024 802	0.029 835
$RMSE_{M6M7}$	0.017 100	0.023 125

TABLE V. Computational times in seconds of the two-layer model for the simulation of the different meshes and two friction assumptions.

	M1	M2	M3	M4	M5	M6	M7
Implicit Friction	1.87	4.14	8.98	21.73	51.11	124.72	334.98
Frictionless	1.84	3.89	8.83	20.43	49.93	129.38	329.25

Finally, Table V shows the computational times used by the model for the simulation on each of the meshes and each of the friction assumptions, for the computation of the 400 s of the test case. The simulation has been performed without parallelization with a single Intel (R) Core i7–8700, and it is observed that the increase in the computation time is proportional to the increase in load, caused by the increase in the number of computation cells. Moreover, the computational increase factor is not exactly the same as the increase factor of the number of cells, but somewhat higher, due to the fact that the increase in the number of cells increases the computational time of extra tasks of the model, such as data dumping or updating and imposing boundary conditions, in which more cells are involved in the finer the mesh. It is also worth mentioning that no noticeable differences can be found between simulation with and without the friction algorithm activated.

D. Wind sensitivity analysis of an oil spill over a coastal area

1. Test case description

This test case is devoted to ensure the proper behavior of the model when dealing with wet-dry fronts and long unsteady simulations. It also serves as a test case to perform sensitivity analysis of the 2D model.

The base of this test case is the computational 2D extension of a 1D laboratory experiment carried out in 1993 in Delft representing the behavior of coastal waves propagation.[47] This experiment setup has been used for the validation of coastal numerical models.[48–52] In this case, its data are scaled and used for the representation of a coastal area where an oil spill might occur.

Regarding the water layer and bottom, all the spatial dimensions of the Delft test case are scaled by 100 and are represented in Fig. 18. In order to create a 2D domain, the profile is projected along the longshore direction until it reaches the same length (L = 3170 m), so the top view of the experiment is a square. In Fig. 19, a representation of the numerical unstructured mesh of the bottom and the water surface elevation can be seen. Note that the inshore boundary condition does not affect the flow, as the terrain elevation is higher than the water surface and the wet/dry front remains within the domain. On the other hand, the onshore boundary condition is the scaled time series of water elevation obtained from the SLN Beji and Battjes experiment over the Delft channel.[47] By doing a dimensional analysis, the spatial variables (i.e., elevation) are multiplied by 100, while the temporal variables (i.e., time) are multiplied by 10. The result is the time water surface elevation series represented in Fig. 20.

The simulation is carried out over a triangular unstructured mesh with an approximated homogeneous distribution of cell sizes. The target area of the triangular elements is set to 500 m^2 in the whole domain. However, it decreases up to 102 m^2 in the smallest element due to the unstructured nature. The simulation runs 10 000 s (2.7 h)

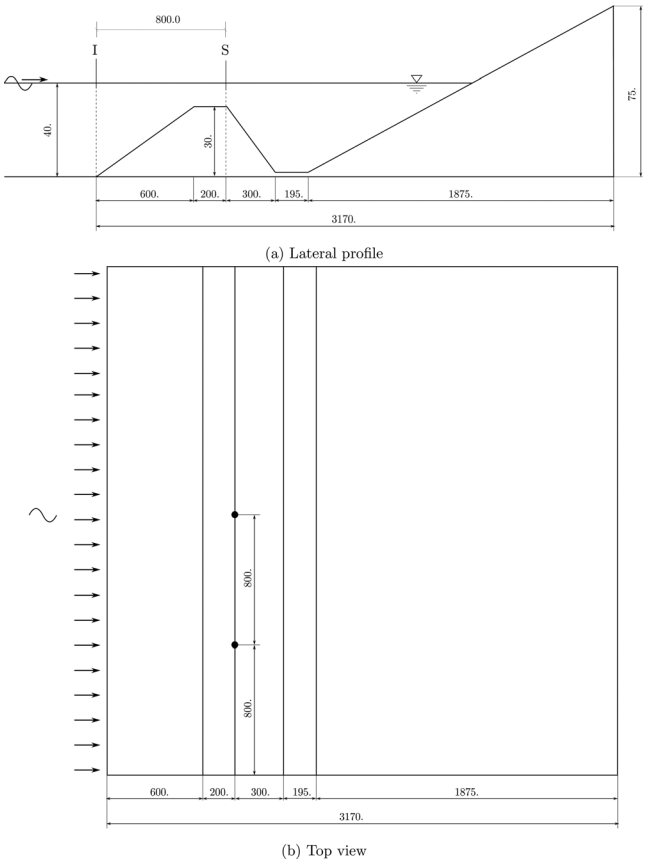

FIG. 18. Lateral profile (a) and top view (b) of the 2D oil spill numerical test case in which two oil sources have been located and represented by a thick point.

with a CFL = 0.9. The Manning number at the seabed is considered $n_b = 0.01$.

On the other hand, the oil is assumed to spill over the water volume by means of a mass source term in Eq. (4a). The spill source is located in two points, whose exact location can be seen in the top view of Fig. 18(b). The mass is introduced within the domain through an additional mass source term in the computational cells where sources are located. The extra water depth added each time step as spill depends on the area of the cell, which have 314.6 and 457.04 m^2, as the given input for the spill is a discharge. The time series of discharge and temperature of the different oil sources for the test case are represented in Fig. 21. Finally, a wind polygon is set affecting all the domain with three different values that are summarized in Table VI.

2. Wind sensitivity analysis

In order to ensure the suitability of the model to handle such oil spill phenomena, challenging numerical test cases must be carried out to test the model wet/dry fronts or the high friction stresses handling.

In this case, three different wind scenarios have been considered to test the numerical stability as well as the influence of this term in the system. Table VI summarizes the parameters chosen for the three subcases.

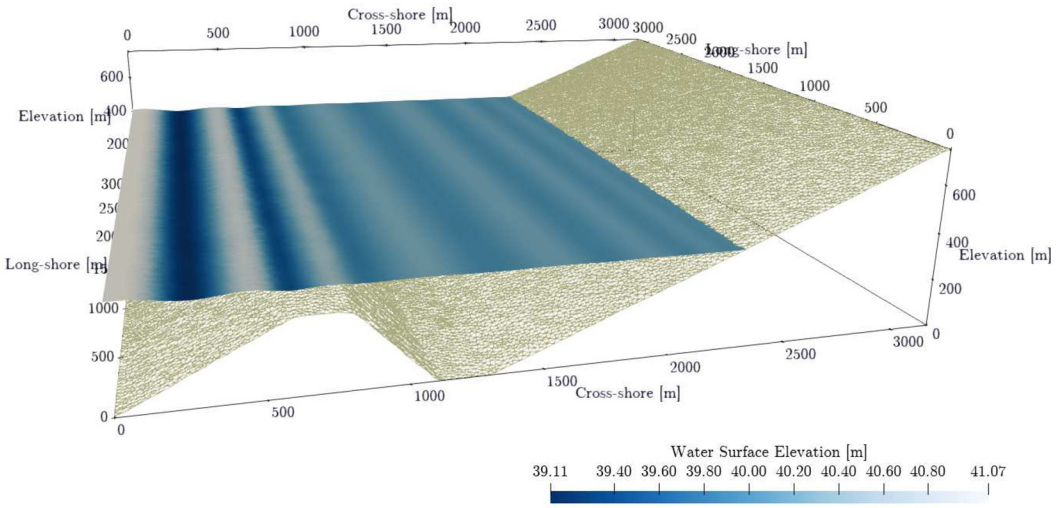

FIG. 19. 3D representation of the bottom and the water surface elevation of the 2D oil spill numerical test case for a random time.

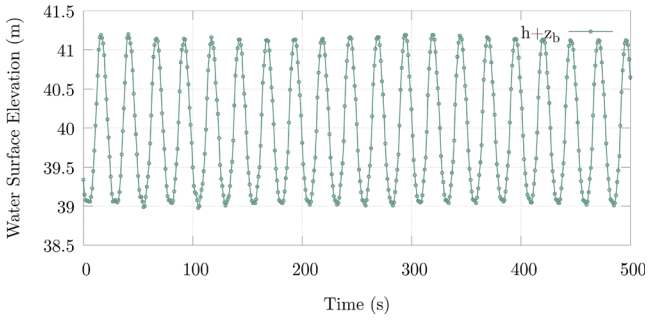

FIG. 20. Time evolution of water surface elevation at the boundary condition for the numerical test case proposed.

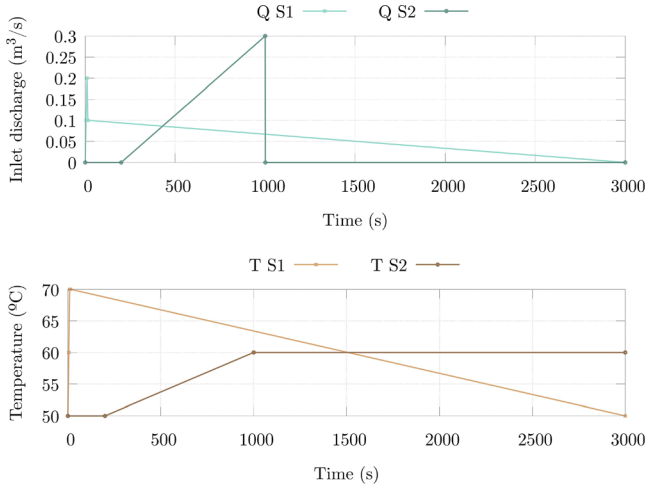

FIG. 21. Time evolution of inlet oil sources in terms of discharge (up) and temperature (down).

TABLE VI. Summary of parameters for the wind sensitivity analysis of the 2D two-layer oil spill model.

Case	x wind (m/s)	y wind	C_a	ρ_a (kg/m^3)
Case 0	0	0	0.01	1.29
Case 1	10	0	0.01	1.29
Case 2	−10	0	0.01	1.29

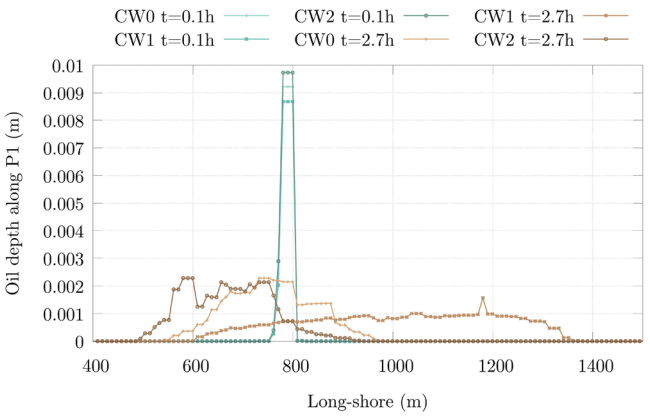

FIG. 22. Oil depth distribution along longshore profile at time t = 0.1 h and t = 2.7 h in the three different wind scenarios proposed.

The model has been specifically designed to handle wet/dry boundaries for simulating such spills. The significance of incorporating the spatial distribution of temperature, density, heat transfer, and wind is evident from the obtained results. Two distinct scenarios were simulated: environment A, characterized by the absence of wind (low convection coefficient), typical air temperature, and solar radiation; and environment B, characterized by high wind speed, low air temperature,

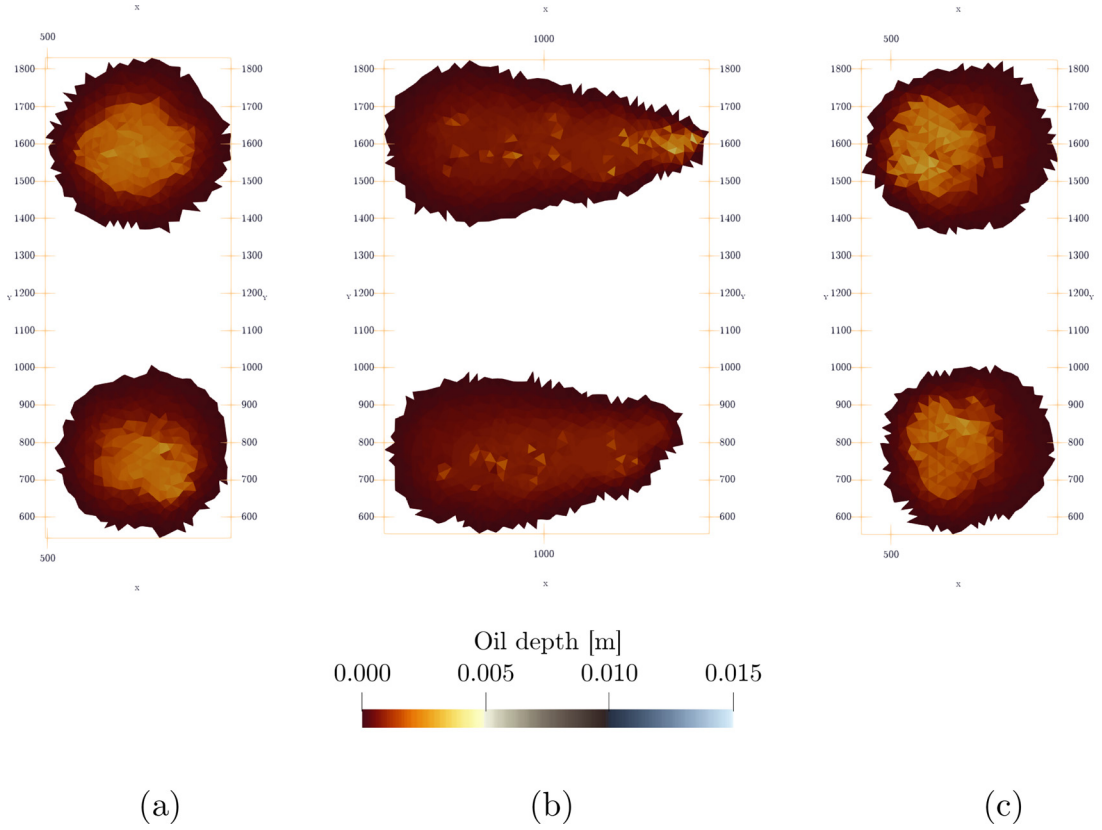

FIG. 23. 2D spatial distribution of oil depth at final time (t = 2.7 h) in the three different wind scenarios proposed: no wind (a), positive wind (b), and negative wind (c).

and no solar radiation. In Fig. 22, a profile of the oil slicks for the three different wind situations can be seen. It can be noted how the wind can govern totally the way in which the oil slick is spread. This is also seen in Fig. 23, where a 2D representation of oil slicks is shown, and in Fig. 24, where spread is seen within a 3D representation with the water layer and the bottom.

The simulation results highlight the importance of considering various environmental factors when modeling oil spills over water. The incorporation of elements, such as temperature, evaporation, heat transfer, and wind, allows for a more comprehensive representation of the complex dynamics involved. It is evident that oil spills can evolve differently under different conditions, and the model's ability to encompass these variations enhances its efficacy in providing a more accurate understanding of potential spill scenarios.

E. Oil spill over coastal-type water volume with land interaction

The objective of this test case is to test together the use of all the mechanisms implemented in the two-layer oil spill model. For this purpose, a spill with the influence of wind, waves, evaporation, and involving not only the release of oil over volumes of water, but also the eventual arrival of the oil on the beach, so that it begins to flow over the land, is simulated.

Figure 25 shows a 3D representation of the computational mesh used for the discretization of the terrain, as well as the representation of the initial water level at rest. The computational mesh is composed of 41176 triangular elements, homogeneously distributed with an area of 6000 m^2 that can decrease up to 1244 m^2. Upon the water initial condition, an oil source is placed on one side, while a temporal variation of level is imposed on the input boundary condition, which introduces monochromatic waves. All other boundaries of the domain are closed.

Additionally, a constant wind is imposed on the whole domain whose components are

$$u_{a,x} = \frac{\sqrt{2}}{2}; \quad u_{a,y} = \frac{\sqrt{2}}{2}, \tag{47}$$

so that the velocity magnitude is 1 m/s. Evaporation is activated, and the model transports not only the temperature, but also the age of the oil since it left the leak point.

The source representing the spill has a time-varying flow rate, shown in Fig. 26, and enters with a time-varying temperature, also plotted in Fig. 26.

The simulation runs for 2.7 h with a CFL of 0.9, and the interface friction is used implicitly to avoid instabilities due to the advance of very small oil depths on the shore. The friction Chezy coefficient between layers is $C = 0.001$, and the Manning coefficient with the bottom is $n = 0.01$.

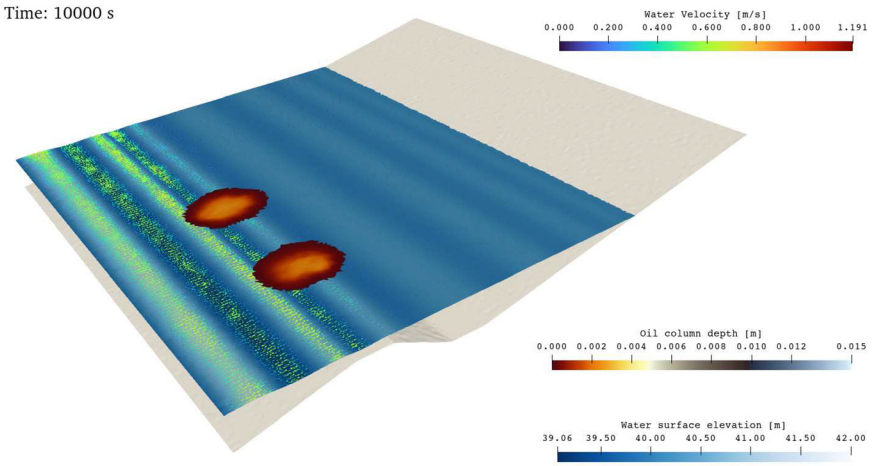

(a) No wind

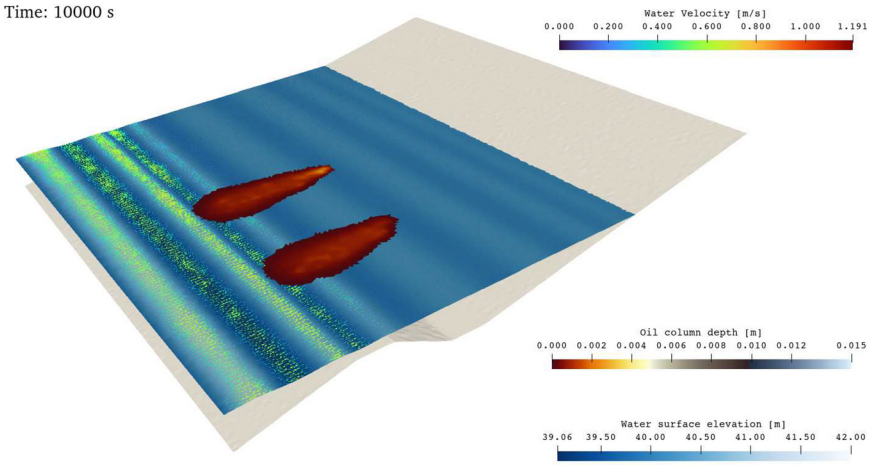

(b) Positive wind of 10 m/s.

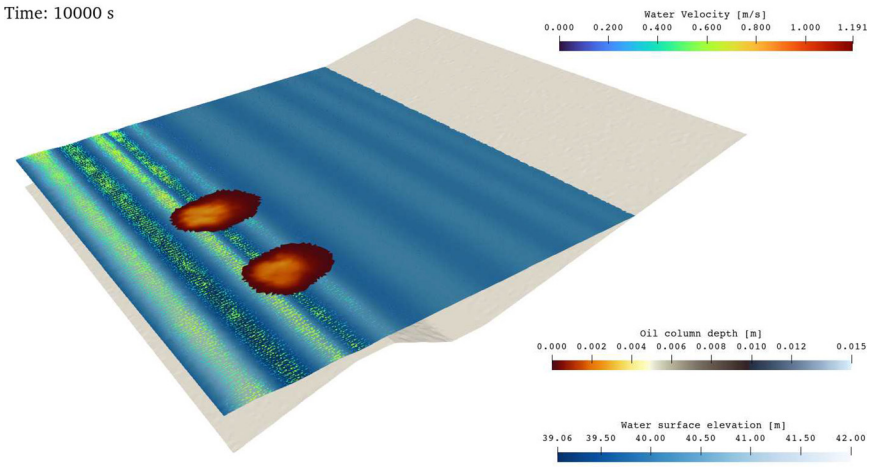

(c) Negative wind of -10 m/s.

FIG. 24. 3D representation of oil spill over the water volume at final time (t = 2.7 h) in the three different wind scenarios proposed: no wind (a), positive wind (b), and negative wind (c).

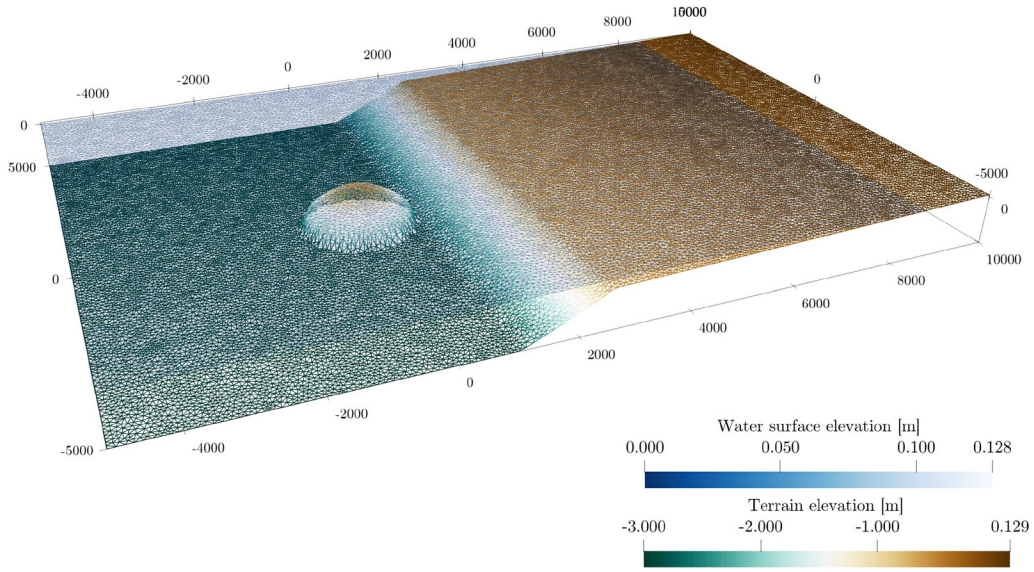

FIG. 25. 3D representation of computational mesh in terrain and water surface elevation of an oil spill on a beach test case.

Figure 27 shows the spatial distribution of the depth and velocity field for the oil layer at different times. In the same figure, the wet cells of water layer have been represented with the mesh wireframe, so that the areas where the oil is advancing over the dry terrain without water underneath can be easily observed. Additionally, the dry terrain is also represented with some transparency and the intersection between oil and the terrain can be detected. Analogous results can be observed in Fig. 28 for oil age and temperature.

The spatial distribution figures show the impact of wind, which forces the oil slick toward the beach and provokes its penetration inland.

The evolution of the slick shows that, although the oil propagates over the coast, the change in the friction law and the magnitude of the friction cause a barrier effect that accumulates the oil on the shore. This behavior, although justifies the existence of a model capable of simulating the evolution of the oil inland, demonstrates that it is not necessary for these cases to use a more complex friction or rheological model.

V. CONCLUSIONS

Oil spills over water volumes can be simulated with two-layer models with the aim of providing the oil layer its own characteristics and rheological behavior, since traditionally it has been only transported as a passive solute or coupled with Lagrangian methods that represent the oil slick as a set of oil particles moving under a given velocity distribution. In this work, a two-layer shallow water type model for oil and water has been implemented with an additional hypothesis: a null pressure effect from the upper oil layer over the thick water volume below. One of the challenges of this models resides on the numerical stability due to the presence of very low oil depths and the presence of wet/dry fronts transporting temperature.

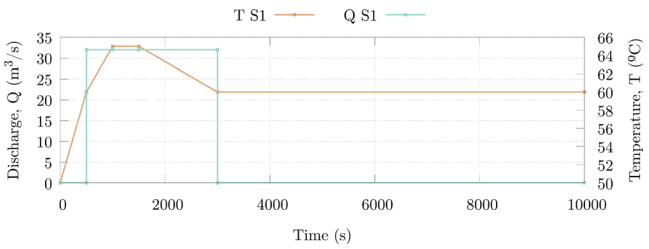

FIG. 26. Time series of inlet sources in terms of discharge and temperature.

The model presented has been validated through reference solutions for steady states with and without the presence of friction stresses. No instabilities have been detected, and a good agreement has been achieved applying the explicit approach for interface friction τ_w. Additionally, a hypothetical oil spill has been simulated to ensure the robust behavior of the model in the presence of wet/dry fronts, strong winds, and temperature evolution. Good results are presented in terms of stability even for a low slick thickness, and the effect of wind has been tested and validated.

An evaluation of the explicit and semi-implicit approaches for friction terms in the oil–water interface has been done with a challenging test case. The semi-implicit approach exhibited a notable advantage in terms of robustness, owing to its unconditionally stable nature, thus outperforming the explicit approach.

This application represents an extreme test case featuring high friction terms and wet/dry fronts that emerged as a challenging scenario wherein the semi-implicit approach was indispensable to avoid instabilities. In other cases, the explicit approach demonstrated satisfactory performance, effectively preserving steady states, which is a limitation of the semi-implicit approach. Consequently, it can be concluded that neither approach can be universally regarded as superior, as each exhibits strengths and weaknesses that make them suitable for specific scenarios. A comprehensive understanding of the strengths and limitations of both approaches is imperative for selecting the most appropriate method tailored to the unique characteristics and complexities of the oil spill scenario under consideration.

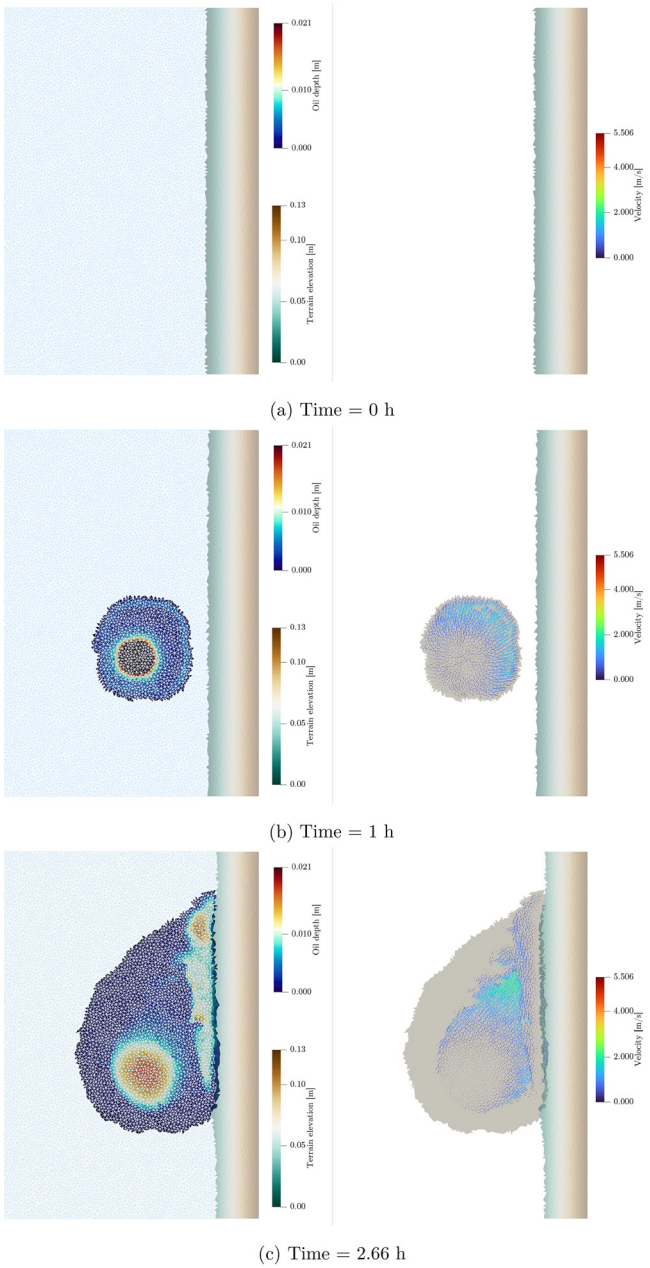

(a) Time = 0 h

(b) Time = 1 h

(c) Time = 2.66 h

FIG. 27. 2D distribution of oil depth (left) and velocity field (right) of an oil spill on a beach at different times.

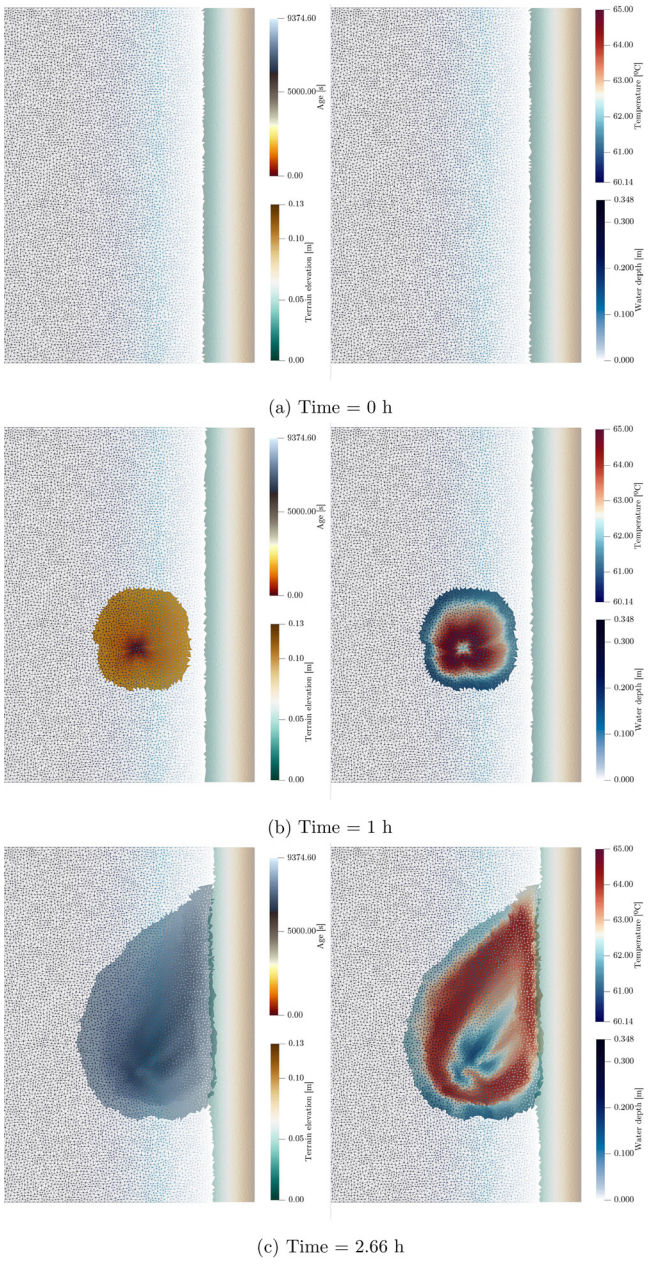

(a) Time = 0 h

(b) Time = 1 h

(c) Time = 2.66 h

FIG. 28. 2D distribution of oil age (left) and temperature field (right) of an oil spill on a beach at different times.

The oil spill model presented in this study incorporates a specific evaporation model to account for the evaporation process in oil spills. While acknowledging the need for further improvements, it is important to note that the existing evaporation model provides a valuable representation of at least some evaporation effects such as the mass loss. The model has been validated in terms of mass conservation. The complexity of oil compositions, which vary across sources and over time, presents challenges in developing precise evaporation equations associated with specific oil types. Given the limited research on oil spill evaporation and the lack of comprehensive data, the current evaporation model serves as a reasonable approximation to introduce the effects of evaporation into the model. Future efforts should focus on refining the evaporation model affecting other rheological variables of the oil with experimental or real cases.

Finally, it is interesting to mention that the aim of the paper focuses on numerical validation of the model, and future

improvements could be done. In particular, in the model in its present form, different types of oil can be represented by means of the parameters defining the dependence of density and viscosity with temperature and the rheological model. However, in future improvements of the model, the oil composition could be divided into volatile and nonvolatile components of different concentration and evaporation affecting only volatile part.

ACKNOWLEDGMENTS

Hydronia Europe S.L. has funded a part of this research by means of an Industrial Doctorate Research Grant No. DIN2018-010036. Additionally, this work was partially funded by Diputación General de Aragón, DGA, through Fondo Europeo de Desarrollo Regional, FEDER.

AUTHOR DECLARATIONS

Conflict of Interest

The authors have no conflicts to disclose.

Author Contributions

Isabel Echeverribar: Conceptualization (equal); Formal analysis (lead); Investigation (lead); Software (lead); Validation (lead); Visualization (equal); Writing – original draft (lead); Writing – review & editing (supporting). **Pilar Brufau:** Conceptualization (equal); Formal analysis (supporting); Investigation (supporting); Software (supporting); Supervision (equal); Validation (supporting); Visualization (equal); Writing – original draft (supporting); Writing – review & editing (equal). **Pilar García-Navarro:** Conceptualization (equal); Formal analysis (supporting); Investigation (supporting); Software (supporting); Supervision (equal); Validation (supporting); Visualization (equal); Writing – original draft (supporting); Writing – review & editing (equal).

DATA AVAILABILITY

The data that support the findings of this study are available from the corresponding author upon reasonable request.

REFERENCES

[1]See https://www.itopf.org/knowledge-resources/data-statistics/statistics/ for "Oil tanker spill statistics (2022)," accessed June 27, 2023.
[2]I. T. O. P. Federation, "Use of booms in oil pollution response," Technical Information Papers - ITOPF (2014), Vol. 3, pp. 1–12.
[3]I. T. O. P. Federation, "Aerial observation of marine oil spills," Technical Information Papers - ITOPF (2014), Vol. 1, pp. 1–12.
[4]J. Reed, M. O, P. J. Brandvik, P. Daling, A. Lewis, R. Fiocco, D. Mackay, and R. Prentki, "Oil spill modeling towards the close of the 20th century: Overview of the state of the art," Spill Sci. Technol. Bull. **5**(1), 3–16 (1999).
[5]P. Tkalich, "A CFD solution of oil spill problems," Environ. Modell. Softw. **21**, 271–282 (2006).
[6]D. P. Hoult, "Oil spreading on the sea," Annu. Rev. Fluid Mech. **4**, 341–368 (1972).
[7]P. Keramea, K. Spanoudaki, G. Zodiatis, G. Gikas, and G. Sylaios, "Oil spill modeling: A critical review on current trends, perspectives, and challenges," J. Mar. Sci. Eng. **9**(2), 181 (2021).
[8]G. Zodiatis, R. Lardner, T. Alves, Y. Krestenitis, L. Perivoliotis, S. Sofianos, and K. Spanoudaki, "Oil spill forecasting (prediction)," J. Mar. Res. **75**, 923–953 (2017).
[9]M. L. Spaulding, "State of art review and future directions in oil spill modeling," Mar. Pollut. Bull. **115**, 7–19 (2017).
[10]C. B. Vreugdenhil, *Numerical Methods for Shallow-Water Flow* (Kluwer Academic Publishers, Dordrecht, The Netherlands, 1994).
[11]V. Casulli and G. S. Stelling, "Numerical simulations of 3D quasi-hydrostatic free-surface flows," J. Hydraul. Eng. **124**, 678–686 (1998).
[12]V. Casulli and P. Zanolli, "Semi-implicit numerical modeling of nonhydrostatic free-surface flows for environmental problems," Math. Comput. Modell. **36**, 1131–1149 (2002).
[13]M. Reed and C. A. O. Turner, "The role of wind and emulsification in modelling oil spill and surface drifter trajectories," Spill Sci. Technol. Bull. **1**(2), 143–157 (1994).
[14]C. Kuang, J. Chen, J. Wang, R. Qin, J. Fan, and Q. Zou, "Effect of wind-wave-current interaction on oil spill in the Yangtze river estuary," J. Mar. Sci. Eng. **11**(3), 494 (2023).
[15]I. Echeverribar, S. Martínez-Aranda, J. Fernández-Pato, and P. García-Navarro, "A GPU-based 2D viscous flow model with variable density and heat exchange," Adv. Eng. Softw. **175**, 103340 (2023).
[16]M. Fingas, *Oil and Petroleum Evaporation* (John Wiley & Sons, Ltd, 2014), Chap. 7, pp. 205–223.
[17]M. F. Fingas, "Studies on the evaporation of crude oil and petroleum products: I. The relationship between evaporation rate and time," J. Hazard. Mater. **56**, 227–236 (1997).
[18]B. Ivorra, S. Gomez, J. Carrera, and A. M. Ramos, "A compositional Eulerian approach for modeling oil spills in the sea," Ocean Eng. **242**, 110096 (2021).
[19]S. Martínez-Aranda, A. Ramos-Pérez, and P. García-Navarro, "A 1d shallow-flow model for two-layer flows based on force scheme with wet-dry treatment," J. Hydroinf. **22**(5), 1015–1037 (2020).
[20]J. Murillo, S. Martínez-Aranda, A. Navas-Montilla, and P. García-Navarro, "Adaptation of flux-based solvers to 2D two-layer shallow flows with variable density including numerical treatment of the loss of hyperbolicity and drying/wetting fronts," J. Hydroinf. **22**(5), 972–1014 (2020).
[21]J. Murillo and P. García-Navarro, "Energy balance numerical schemes for shallow water equations with discontinuous topography," J. Comput. Phys. **236**(1), 119–142 (2013).
[22]J. Murillo and P. García-Navarro, "Weak solutions for partial differential equations with source terms: Application to the shallow water equations," J. Comput. Phys. **229**(0), 4327–4368 (2010).
[23]I. Echeverribar, M. Morales-Hernández, P. Brufau, and P. García-Navarro, "2D numerical simulation of unsteady flows for large scale floods prediction in real time," Adv. Water Resources **134**, 103444 (2019).
[24]J. Murillo, P. Garcia-Navarro, J. Burguete, and P. Brufau, "The influence of source terms on stability, accuracy and conservation in two-dimensional shallow flow simulation using triangular finite volumes," Int. J. Numer. Methods Fluids **54**(5), 543–590 (2007).
[25]J. Burguete, P. García-Navarro, J. Murillo, and I. García-Palacín, "Analysis of the friction term in the one-dimensional shallow-water model," J. Hydraul. Eng. **133**(9), 1048–1063 (2007).
[26]J. Burguete, P. García-Navarro, and J. Murillo, "Friction term discretization and limitation to preserve stability and conservation in the 1d shallow-water model: Application to unsteady irrigation and river flow," Int. J. Numer. Methods Fluids **58**(4), 403–425 (2008).
[27]L. Cea and E. Bladé, "A simple and efficient unstructured finite volume scheme for solving the shallow water equations in overland flow applications," Water Resources Res. **51**(7), 5464–5486 (2015).
[28]G. Arcement and V. Schneider, "Guide for selecting Manning's roughness coefficients for natural channels and flood plains," No. 2339 in U.S. Geological Survey. Water-supply paper, 1984.
[29]V. T. Chow, *Open-Channel Hydraulics, McGraw-Hill Civil Engineering Series* (McGraw-Hill, 1959).
[30]F. Palmeri, F. Silván, I. Prieto, M. Balboni, and I. García-Mijangos, *Manual de Técnicas de Ingeniería Naturalística en Ámbito Fluvial, Departamento de Ordenación Del Territorio y Medio Ambiente* (Gobierno del País Vasco, España, 2002).
[31]B. W. P. Staff, G. Witheridge, and B. Q. C. Council, "Natural channel design guidelines," Appendix C, Technical Document, Brisbane City Council, 2000.
[32]G. K. Batchelor, *An Introduction to Fluid Dynamics*, Cambridge Mathematical Library (Cambridge University Press, 2000).

[33]L. M. Jiji, *Heat Convection* (Springer, 2006).
[34]D. G. Kröger, "Convection heat transfer between a horizontal surface and the natural environment," R&D J. **18**(3), 49–54 (2002).
[35]M. F. Fingas, "A literature review of the physics and predictive modelling of oil spill evaporation," J. Hazard. Mater. **42**(2), 157–175 (1995).
[36]E. Toro and P. Garcia-Navarro, "Godunov-type methods for free-surface shallow flows: A review," J. Hydraul. Res. **45**(6), 736–751 (2007).
[37]E. F. Toro, *Riemann Solvers and Numerical Methods for Fluid Dynamics* (Springer, Berlin, 1997).
[38]J. Murillo and P. García-Navarro, "Wave Riemann description of friction terms in unsteady shallow flows: Application to water and mud/debris floods," J. Comput. Phys. **231**, 1963–2001 (2012).
[39]F. J. Leveque, *Finite Volume Methods for Hyperbolic Problems* (Cambridge University Press, New York, 2002).
[40]J. Mairal, J. Murillo, and P. García-Navarro, "The entropy fix in augmented Riemann solvers in presence of source terms: Application to the shallow water equations," Comput. Methods Appl. Mech. Eng. **417**, 116411 (2023).
[41]S. Martínez-Aranda, J. Murillo, M. Morales-Hernández, and P. García-Navarro, "Novel discretization strategies for the 2D non-Newtonian resistance term in geophysical shallow flows," Eng. Geol. **302**, 106625 (2022).
[42]C. Swartenbroekx, Y. Zech, and S. Soares-Frazão, "Two-dimensional two-layer shallow water model for dam break flows with significant bed load transport," Int. J. Numer. Methods Fluids **73**, 477–508 (2013).
[43]R. LeVeque, *Numerical Methods for Conservation Laws, Lectures in Mathematics* (ETH Zürich, Birkhäuser Basel, 1992).
[44]M. Morales-Hernández, J. Murillo, and P. García-Navarro, "Diffusion-dispersion numerical discretization for solute transport in 2D transient shallow-flows," Environ. Fluid Mech. **19**, 1217–1234 (2019).
[45]I. MacDonald, "Analysis and computation of steady open channel flow," Ph.D. thesis (University of Reading, Reading, UK, 1996).
[46]J. R. Shewchuk, "Triangle: Engineering a 2D quality mesh generator and Delaunay triangulator," in *Applied Computational Geometry: Towards Geometric Engineering*, Vol. 1148 of Lecture Notes in Computer Science, edited by M. C. Lin and D. Manocha (Springer-Verlag, 1996), pp. 203–222, from the First ACM Workshop on Applied Computational Geometry.
[47]A. Beji and J. A. Battjes, "Experimental investigation of wave propagation over a bar," Coastal Eng. **19**, 151–162 (1993).
[48]A. Beji and J. A. Battjes, "Numerical simulation of nonlinear wave propagation over a bar," Coastal Eng. **23**, 1–16 (1994).
[49]M. Dingemans, Comparison of computations with Boussinesq-like models and laboratory measurements, Mast-G8M. Note, H1684. Delft Hydraulics (1994).
[50]C. Escalante, T. Morales de Luna, and M. J. Castro, "Non-hydrostatic pressure shallow flows: GPU implementation using finite volume and finite difference scheme," Appl. Math. Comput. **338**, 631–659 (2018).
[51]C. Escalante, M. Dumbser, and M. J. Castro, "An efficient hyperbolic relaxation system for dispersive non-hydrostatic water waves and its solution with high order discontinuous Galerkin schemes," J. Comput. Phys. **394**, 385–416 (2019).
[52]I. Echeverribar, P. Brufau, and P. García-Navarro, "Extension of a roe-type Riemann solver scheme to model non-hydrostatic pressure shallow flows," Appl. Math. Comput. **440**(2), 127642 (2023).